

# Bandpass mismatch error for satellite CMB experiments I: Estimating the spurious signal

**Duc Thuong Hoang,<sup>a,b</sup> Guillaume Patanchon,<sup>a</sup> Martin Bucher,<sup>a,c</sup> Tomotake Matsumura,<sup>d,e</sup> Ranajoy Banerji,<sup>a</sup> Hirokazu Ishino,<sup>f</sup> Masashi Hazumi,<sup>g,e,d,h</sup> Jacques Delabrouille<sup>a,i</sup>**

<sup>a</sup>Laboratoire Astroparticule et Cosmologie (APC), Université Paris Diderot, CNRS/IN2P3, CEA/Irfu, Observatoire de Paris, Sorbonne Paris Cité, 10, rue Alice Domon et Léonie Duquet, 75205 Paris Cedex 13, France

<sup>b</sup>Department of Space and Aeronautics, University of Science and Technology of Hanoi (USTH), Vietnam Academy of Science and Technology, 18 Hoang Quoc Viet, Cau Giay District, Hanoi, Vietnam

<sup>c</sup>Astrophysics and Cosmology Research Unit, School of Mathematics, Statistics and Computer Science, University of KwaZulu-Natal, Durban 4041, South Africa

<sup>d</sup>Kavli Institute for the Physics and Mathematics of the Universe (Kavli IPMU, WPI), UTIAS, The University of Tokyo, Kashiwa, Chiba 277-8583, Japan

<sup>e</sup>Institute of Space and Astronautical Science (ISAS), Japan Aerospace Exploration Agency (JAXA), Sagami-hara, Kanagawa 252-0222, Japan

<sup>f</sup>Department of Physics, Okayama University, 3-1-1 Tsushimanaka, Kita-ku, Okayama 700-8530, Japan

<sup>g</sup>High Energy Accelerator Research Organization (KEK), Tsukuba, Ibaraki 305-0801, Japan

<sup>h</sup>The Graduate University for Advanced Studies (SOKENDAI), Miura District, Kanagawa 240-0115, Hayama, Japan

<sup>i</sup>Département d'Astrophysique, CEA Saclay DSM/Irfu, 91191 Gif-sur-Yvette, France

**Abstract.** Future Cosmic Microwave Background (CMB) satellite missions aim to use the  $B$  mode polarization to measure the tensor-to-scalar ratio  $r$  with a sensitivity  $\sigma_r \lesssim 10^{-3}$ . Achieving this goal will not only require sufficient detector array sensitivity but also unprecedented control of all systematic errors inherent to CMB polarization measurements. Since polarization measurements derive from differences between observations at different times and from different sensors, detector response mismatches introduce leakages from intensity to polarization and thus lead to a spurious  $B$  mode signal. Because the expected primordial  $B$  mode polarization signal is dwarfed by the known unpolarized intensity signal, such leakages could contribute substantially to the final error budget for measuring  $r$ . Using simulations we estimate the magnitude and angular spectrum of the spurious  $B$  mode signal resulting from bandpass mismatch between different detectors. It is assumed here that the detectors are calibrated, for example using the CMB dipole, so that their sensitivity to the primordial CMB signal has been perfectly matched. Consequently the mismatch in the frequency bandpass shape between detectors introduces differences in the relative calibration of galactic emission components. We simulate this effect using a range of scanning patterns being considered for future satellite missions. We find that the spurious contribution to  $r$  from reionization bump on large angular scales ( $\ell < 10$ ) is  $\approx 10^{-3}$  assuming large detector arrays and 20 percent of the sky masked. We show how the amplitude of the leakage depends on the angular coverage per pixels that results from the scan pattern.

**Keywords:** cosmology: observations – cosmic background radiation

---

## Contents

<b>1</b>	<b>Introduction</b>	<b>1</b>
<b>2</b>	<b>Sky emission model and mismatch errors</b>	<b>2</b>
<b>3</b>	<b>Calculating the bandpass mismatch</b>	<b>5</b>
3.1	Results	8
3.2	Analytic estimates	14
3.3	Importance of avoiding resonances	18
3.4	Hitcount and crossing moment map properties	21
<b>4</b>	<b>Conclusions</b>	<b>25</b>

---

## 1 Introduction

Measurements of the cosmic microwave background (CMB) provide a rich data set for studying cosmology and astrophysics and for placing stringent constraints on cosmological models. In particular, the ESA Planck satellite mission has produced full sky maps in both temperature and polarization at unprecedented sensitivity in nine broad ( $\Delta\nu/\nu \approx 0.3$ ) microwave frequency bands [1].

Conventional cosmological models predict that the CMB is linearly polarized, so that the fourth Stokes parameter  $V$  vanishes. CMB polarization patterns can be decomposed in two components known as the  $E$  and  $B$  modes, respectively of even and odd parity. In linear cosmological perturbation theory, *scalar* perturbations produce  $E$  mode polarization but are unable to produce any  $B$  mode polarization at linear order. The  $E$  mode polarization angular power spectrum can be predicted from a model fitted to the measured  $T$  anisotropies. The WMAP [2] and Planck [3] space missions, complemented on smaller angular scales by ACT [4] and SPT [5], have already measured the  $E$  mode polarization power spectrum up to high multipole number  $\ell$ , even if the accuracy of the measurement can still be substantially improved. On the other hand, the odd parity (or pseudo-scalar) polarization pattern called the  $B$  mode arises either from primordial tensor perturbations, or equivalently primordial gravitational waves, presumably generated during inflation, or from scalar modes at higher nonlinear order, primarily through gravitational lensing. Gravitational lensing  $B$  modes dominate over primordial  $B$  modes on small angular scales. These gravitational lensing  $B$  modes have already been observed at  $\ell \gtrsim 100$  by the POLARBEAR [6], SPT-Pol [7] and Bicep2/Keck [8] ground-based experiments. Primordial  $B$  modes have not been observed yet. Their predicted shape features a ‘recombination bump’ visible at  $\ell \approx 80$ , and a ‘reionization bump’ at  $\ell \lesssim 10$ . The overall amplitude of this primordial B-mode spectrum depends linearly on the value of the tensor-to-scalar ratio  $r$ . The current upper limit is  $r < 0.07$  at 95% c.l. [9, 10].

After Planck, a number of ground-based and balloon-borne experiments currently either taking data or in the planning stage aim to make the first detection of primordial  $B$  modes. In parallel, the space-borne mission concepts CORE [11], LiteBIRD [12, 13], and PIXIE [14] have been designed to probe  $B$  modes at higher sensitivities and using frequency bands inaccessible from the ground. Constraining physically-motivated inflation models requires sensitivities in the tensor-to-scalar ratio of  $\sigma_r \lesssim 10^{-3}$ , almost two orders of magnitude beyond the Planck

sensitivity. Furthermore, systematic errors must be controlled so that their contribution to the final error budget is subdominant. The calibration requirements become correspondingly more stringent, and future experiments will have to devise novel calibration procedures to characterize the instrument at a level that makes it possible to correct the raw data at sufficient accuracy.

Typically experiments observe in a number of different frequency channels with many detectors for each frequency channel. Ideally, all detectors in a single channel should have the exact same bandpass function (i.e the response  $g(\nu)$  that defines the transmission of the system as a function of frequency) in order to construct single band maps, which are then analyzed to isolate the primordial cosmological signal. Many detectors are necessary in each channel to improve on the sensitivity of current observations, which already use detectors that are very nearly at the quantum noise limit. If however the detectors that are meant to be identical have slightly different bandpasses, artifacts are introduced into maps that are obtained by combining the signals from several detectors. After cross-calibration on the CMB, for instance using the bright CMB dipole, the amplitude of other astrophysical components is different in the different detectors, and residuals of the differences of integrated intensity project onto the reconstructed polarization maps. Such effects have been observed in Planck [15] and WMAP [16]. In this paper we call these artifacts ‘bandpass mismatch errors’.

Obviously, such errors can be avoided if the observing strategy allows first to make polarization maps with each detector independently, hence without bandpass mismatch errors, and then to combine these individual detector maps into a global map. This however requires observing each sky pixel with enough independent orientations of the detector polarizer. This polarization modulation can be achieved either with the use of a rotating half-wave plate (HWP), or by rotating the whole instrument so that each pixel is observed with an optimized set of detector orientations. However, practical considerations may constrain the range of possible polarization orientations, leading to a loss of sensitivity after combining single detector polarization maps.

The objective of this paper is to evaluate the level of the bandpass mismatch effect for future space missions, and to estimate its possible impact on the final determination of the tensor-to-scalar ratio  $r$  if no correction measures are taken. Our study first focuses on the case without a HWP, and we also verify that the effect is greatly reduced with an ideal rotating HWP without any achromaticity or other non-idealities. For a more detailed discussion of general issues pertaining to the use of a HWP for achieving polarization modulation and in particular a discussion of the issue of achromaticity, we refer the reader to the results of the ABS experiment [17] and the thesis [18] and references therein. We note that in the first case, making single detector maps that are subsequently combined to avoid band-pass mismatch errors, could be done at the price of increased final noise since the angular coverage in each pixel is sub-optimal. HWP non-idealities are not studied in this paper.

In Sect. 2 we model the bandpass mismatch effect, and in Sect. 3 we evaluate the impact on  $B$  mode measurements and relate the mismatch errors to the "crossing moment maps", that provide a measure of uniformity of polarizer angle coverage in each pixel. Correction methods are developed in a companion publication [19].

## 2 Sky emission model and mismatch errors

The total intensity of the microwave sky can be expressed as a sum of components of different astrophysical origin. In intensity, the CMB anisotropies are dominant over most of the sky,

but several diffuse components of Galactic origin are also present as well as compact sources, which include extragalactic radio sources, IR sources (understood to be dusty galaxies), and Sunyaev-Zeldovich (SZ) distortions from the hot gas within galaxy clusters. We model the unpolarized sky emission at position  $\hat{p}$  and frequency  $\nu$  as

$$I_{\text{tot}}(\hat{p}, \nu) = I_0(\nu) + \left. \frac{\partial B(\nu; T)}{\partial T} \right|_{T_0} \Delta T_{\text{CMB}}(\hat{p}) + \sum_{(c)} I_{(c)}(\hat{p}, \nu) \quad (2.1)$$

where  $B(\nu; T)$  is the spectrum of a blackbody at temperature  $T$ ,  $T_0$  is the average CMB temperature of about 2.7255 K,  $\Delta T_{\text{CMB}}(\hat{p})$  is the CMB temperature fluctuation around this mean value,  $I_{(c)}(\hat{p}, \nu)$  the emission spectrum of component  $(c)$  as a function of electromagnetic frequency  $\nu$ ,  $I_0(\nu)$  is the monopole including all components. We have similar relationships for the  $Q$  and  $U$  Stokes parameters. All three Stokes parameters of the CMB at a given position on the celestial sphere have the factorized frequency dependence as given above. A similar factorizable form can be used for the SZ emission assuming that the hot gas is non-relativistic. The galactic components are more complicated at the accuracy required for future satellite missions and an Ansatz where the frequency dependence of each component factorizes out breaks down. However for studying bandpass mismatch error to first order, a simple factorizable model suffices.

For this bandpass mismatch study, we consider only the CMB and the diffuse galactic components, which contribute the largest bandpass mismatch effects. At frequencies  $\approx 150$  GHz where we focus our study, the galactic emission can be decomposed into thermal dust emission, which is the dominant component, and synchrotron, free-free, and spinning dust emissions. The carbon monoxide (CO) rotational emission at transition line frequencies  $\nu = 115$  GHz for  $J = 1 \rightarrow 0$  and  $\nu = 230$  GHz for  $J = 2 \rightarrow 1$  was a source of significant leakage in Planck experiment [20], but is not considered here because we anticipate that the filters used by future satellite experiments will avoid these lines.

For our study we assume that the galactic thermal dust emission is a greybody of temperature  $T_d \approx 19.7$  K [21] with an emissivity spectral index  $\beta(\hat{p})$ , which depends on sky position and whose average value is  $\approx 1.62$  as measured by Planck [21, 22]. The synchrotron and free-free emissions can be described by power law spectra with the negative spectral indices  $\approx -3.1$  and  $\approx -2.3$ , respectively (see [23] and references therein). The fluctuation of the signal (relatively to the average CMB monopole) measured by the detector  $i$  is given by

$$\int d\nu g_i(\nu) \left( I(\hat{p}, \nu) - I_0(\nu) \right) = \int d\nu g_i(\nu) \left. \frac{\partial B(\nu; T)}{\partial T} \right|_{T_0} \Delta T_{\text{CMB}}(\hat{p}) + \int d\nu g_i(\nu) I_d(\hat{p}, \nu_0) \left( \frac{\nu}{\nu_0} \right)^{\beta(\hat{p})} \frac{B(\nu; T_d)}{B(\nu_0; T_d)} + \dots, \quad (2.2)$$

where  $I_0(\nu) = B(\nu; T_0)$  is the CMB monopole,  $g_i(\nu)$  is the bandpass function of the detector  $i$ ,  $I_d(\hat{p}, \nu_0)$  is the amplitude of the dust component at the reference frequency  $\nu_0$ , and where the dots stand for other components (such as synchrotron and free-free) not explicitly written here. To first order we obtain for the total sky intensity  $I_{\text{sky}}(\nu_0)$  after converting the CMB temperature  $\Delta T_{\text{CMB}}$  to intensity  $I_{\text{CMB}}(\nu_0)$ :

$$I_{\text{sky}}(\nu_0) = I_{\text{CMB}}(\nu_0) + \gamma_d I_{\text{dust}}(\nu_0) + \gamma_s I_{\text{sync}}(\nu_0) + \dots, \quad (2.3)$$

where

$$\gamma_d = \left( \frac{\int d\nu g_i(\nu) \left( \frac{\nu}{\nu_0} \right)^\beta \frac{B(\nu; T_d)}{B(\nu_0; T_d)}}{\int d\nu g_i(\nu) \left( \frac{\partial B(\nu; T)}{\partial T} \right) \Big|_{T_0}} \right) \left( \frac{\partial B(\nu_0; T)}{\partial T} \right) \Big|_{T_0}. \quad (2.4)$$

The factor  $\gamma_s$  is similarly defined integrating over the synchrotron spectrum, etc.

Eqn. (2.3) also holds for the polarization when  $I$  is replaced with  $Q$  and  $U$ . The unit normalization for the CMB component is justified because the data are calibrated using the CMB dipole (or higher order temperature anisotropies). The values of the  $\gamma$  parameters are close to unity when the bandwidth is narrow.

Differences in the bandpass function  $g_i(\nu)$  from detector to detector result in corresponding variations in  $\gamma$  from detector to detector for each non-CMB component. Such variations have been observed in Planck data (see Figs. 5 and 28 of [24] for the measured Planck filters and the mismatch parameters, respectively). Pre-flight Fourier Transform Spectrometer (FTS) ground measurements characterized variations of the filter edge positions at both the low and high frequencies at about the percent level. Ground measurements, however, were not accurate enough to detect variations near the center of the filters, and thus could not be used to determine the  $\gamma$  parameters with sufficient accuracy. The  $\gamma$  parameter variations had to be determined from flight data to allow an accurate correction of the leakage (see the low- $\ell$  Planck paper [15] as well as [25]). It should be noted that the variations of the bandpass functions of the filters from detector to detector for a future satellite experiment will depend on the kind of detector technology used (see also [26] regarding the WMAP experiment).

As already stressed, for the above sky emission model where each component has a fixed (factorizable) frequency dependence, the bandpass mismatch maps depend only on the  $\gamma$  parameters and not on the other details of the filters. The deviations from this simplified model due to the observed spatial variations of the spectral indices of component spectra and of thermal dust temperature produce a second order correction to the bandpass mismatch effect, which is neglected for this study. Consequently, the intensity to polarization leakage due to bandpass mismatch can be obtained using only the  $\gamma$ 's and no additional properties of the bandpass functions.

To relate these variations to filter properties, we assume a simple model in which each frequency band is a tophat bandpass function for which  $g(\nu) = 1$  in the interval  $[\nu_{\min}, \nu_{\max}]$  and  $g(\nu) = 0$  elsewhere. We assume that the variations in  $\nu_{\min}$  and  $\nu_{\max}$  for each detector are generated independently according to a uniform distribution with a width of 1%.<sup>1</sup>

We also assume a bandwidth  $(\nu_{\max} - \nu_{\min})/\nu_0$  of 0.25 on average, with  $\nu_0 = 140.7$  GHz. The resulting RMS of  $\gamma_d$  is 0.6% for this simple model. This is similar to the variations observed for Planck at 143 GHz. The fact that actual bandpass functions are more complex functions of  $\nu$  does not affect the applicability of the present work as long as the corresponding  $\gamma$  coefficients remain of the same order of magnitude. Results for other values may be obtained by trivial rescaling. We verified the expected linear scaling by increasing the width of the

---

<sup>1</sup> We thank Aritoki Suzuki for sharing with us that the measurement errors with FTS in the bandpass of the third-order Chebyshev filter placed between the broadband sinuous antennas and the bolometers of the focal plane panels of the Simons Array [27] give approximately this spread. Obviously, since these are values dominated by measurement error, the actual bandpass mismatch for these filters could be much smaller. These measurements merely serve to establish an upper bound on the mismatch. These values are also of the same order of magnitude as the values representing the bandpass mismatch of the metal mesh filters used as part of the Planck satellite HFI instrument. [See [28] for a discussion of the Planck bandpass mismatch.]

uniform distribution from 1% to 2% and observed that the leakage increases by a factor of 2, as expected.

This simple model for detector bandpasses is appropriate for the foreground components having a smooth frequency spectral dependence (e.g., synchrotron and dust emission), but for galactic line emission (such as galactic CO emission and other spectral lines) a more detailed model would be required. The  $\gamma$ 's are computed as a random set from this distribution model, since those are the only quantities needed for the bandpass mismatch evaluation.

In this paper, we focus our analysis on a frequency channel centered at  $\nu_0 = 140$  GHz, and so we restrict ourselves to the dominant galactic component, namely the thermal dust emission. More galactic components are included in the companion paper discussing the correction of the mismatch [19].

### 3 Calculating the bandpass mismatch

In this Section we use a simplified model of the measurement, stripped of additional complications such as asymmetric beams, pixelization effects, etc. for estimating the dominant contribution to the bandpass mismatch error. A study of more than one source of systematic errors simultaneously would obviously be more complicated and also less intuitive to interpret. Here our purpose is to study bandpass mismatch error in isolation and in the simplest possible context.

We assume a scanning pattern that combines three rotations: a relatively fast spin of the payload, around a spin axis that precesses around the anti-solar direction, which itself follows the yearly motion of the spacecraft around the Sun. Many of the proposed future CMB polarization space missions have adopted such a scan strategy [11, 13, 29]. The exact scanning pattern is characterized by the following parameters:  $\alpha$  (precession angular radius),  $\beta$  (spin angular radius),  $\tau_{\text{prec}}$  (precession period), and  $\tau_{\text{spin}}$  (spin period). The motion of the satellites and the definitions of the scanning parameters are indicated in Figure 1.

Our simulations use maps of the celestial sphere pixelized using HEALPix<sup>2</sup> [30] (with  $n_{\text{side}} = 256$ ). A sufficiently fast sampling rate is chosen so that several hits are recorded during each pixel crossing, so that altering this parameter does not significantly affect the results. White instrument noise of a stationary amplitude is assumed, and under this hypothesis, we solve the map making equation:

$$\hat{\mathbf{m}} = (\mathbf{A}^T \mathbf{N}^{-1} \mathbf{A})^{-1} (\mathbf{A}^T \mathbf{N}^{-1} \mathbf{d}). \quad (3.1)$$

Here the notation is such that  $\hat{\mathbf{m}}$  includes the estimated maps of Stokes parameters  $\hat{I}$ ,  $\hat{Q}$  and  $\hat{U}$ ;  $\mathbf{A}$  is the pointing matrix relating data samples to map;  $\mathbf{N}$  is the noise covariance matrix in the time domain; and we denote the polarization angle of a detector  $\psi$  with respect to a reference axis. Individual measurements comprising the data vector  $\mathbf{d}$  are given by

$$S_j = I(p) + Q(p) \cos 2\psi_j + U(p) \sin 2\psi_j + n_j \quad (3.2)$$

where  $n_j$  represents a stationary white noise source for observations indexed by  $j$ . Here the index  $j$  ( $j = 1, \dots, N_p$ ) labels the observations falling into the pixel labelled by  $p$ . The normalization of the noise does not matter for our purpose. The model here assumes that all the beams are azimuthally symmetric and identical.

---

<sup>2</sup><http://healpix.sourceforge.net>

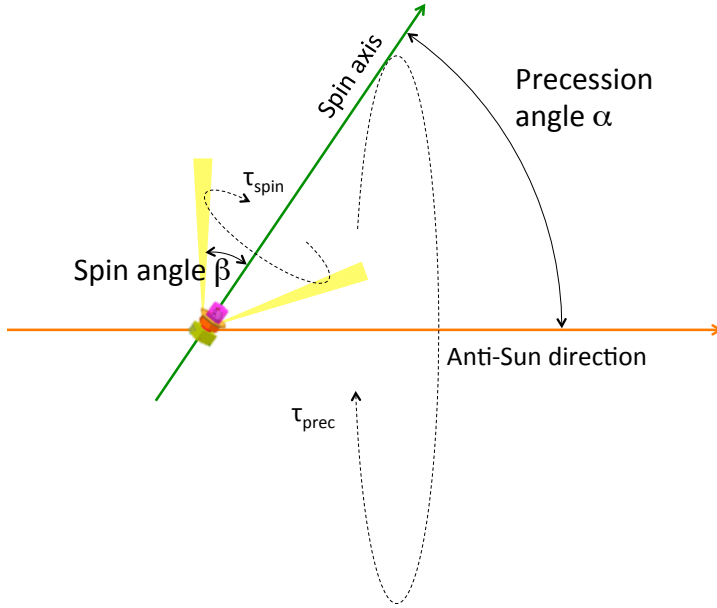


**Figure 1.** Representation of typical satellite scanning strategy.

The hypothesis of white instrument noise provides considerable simplification because in this special case the map making equation [i.e., eqn. (3.1)] can be cast into a block diagonal form, so that the equations for different pixels decouple from each other. Each block (labelled by the pixel index  $p$ ) takes the form

$$\begin{pmatrix} \hat{I}(p) \\ \hat{Q}(p) \\ \hat{U}(p) \end{pmatrix} = \frac{1}{N_p} \times \begin{pmatrix} 1 & \langle \cos 2\psi_j \rangle & \langle \sin 2\psi_j \rangle \\ \langle \cos 2\psi_j \rangle & \frac{1 + \langle \cos 4\psi_j \rangle}{2} & \frac{\langle \sin 4\psi_j \rangle}{2} \\ \langle \sin 2\psi_j \rangle & \frac{\langle \sin 4\psi_j \rangle}{2} & \frac{1 - \langle \cos 4\psi_j \rangle}{2} \end{pmatrix}^{-1} \\
 \times \begin{pmatrix} \sum_j S_j \\ \sum_j S_j \cos 2\psi_j \\ \sum_j S_j \sin 2\psi_j \end{pmatrix} \quad (3.3)$$

where the hats indicate the maximum likelihood estimator, and  $\langle \cdot \rangle$  denotes the average of a quantity over all data samples  $j$ .

Computing the maps  $\hat{I}(p)$ ,  $\hat{Q}(p)$ , and  $\hat{U}(p)$  as above gives the minimum variance estimator of the sky signal in the frequency band under consideration under the hypothesis that the noise of each detector is white (with no correlation in time giving rise to excess low-frequency noise, nor variation of the noise r.m.s. with time), that it is uncorrelated between detectors, and that its level is identical in all detectors [31]. It also assumes no source of systematic errors which may require a different detector weighting to estimate each of the Stokes parameters (and, in particular, no bandpass mismatch).



Following Equation 3.2, for this map-making solution, bandpass mismatch causes the following map errors

$$\begin{pmatrix} \delta \widehat{I}_{BPM} \\ \delta \widehat{Q}_{BPM} \\ \delta \widehat{U}_{BPM} \end{pmatrix} = \begin{pmatrix} 1 & \langle \cos 2\psi_j \rangle & \langle \sin 2\psi_j \rangle \\ \langle \cos 2\psi_j \rangle & \frac{1 + \langle \cos 4\psi_j \rangle}{2} & \frac{\langle \sin 4\psi_j \rangle}{2} \\ \langle \sin 2\psi_j \rangle & \frac{\langle \sin 4\psi_j \rangle}{2} & \frac{1 - \langle \cos 4\psi_j \rangle}{2} \end{pmatrix}^{-1} \times \begin{pmatrix} \delta \langle S_j \rangle \\ \delta \langle S_j \cos 2\psi_j \rangle \\ \delta \langle S_j \sin 2\psi_j \rangle \end{pmatrix} \quad (3.4)$$

where  $\delta \langle S_j \rangle$ ,  $\delta \langle S_j \cos 2\psi_j \rangle$ , and  $\delta \langle S_j \sin 2\psi_j \rangle$  are functions of the underlying sky component maps. Here we assume that the normalization of the CMB component for each detector is perfect. This is obviously an idealization because in reality there are also systematic errors from uncorrected gain variation, but this is a separate issue that we do not analyze here. Moreover, since the relative gain of the detectors is calibrated using the CMB dipole, the approximation that the error is mostly in the relative contributions of the other components is a reasonable one.

Given a model of the microwave sky, the bandpass functions of the various detectors, and the scanning pattern on the sky, eqn. (3.4) can be used to compute the bandpass mismatch errors in the reconstruction of a map of Stokes parameters. For future studies of the CMB polarization, and in particular for the search for primordial  $B$  modes, the error of greatest concern arises from the leakage of the  $I$  component of the foregrounds into the  $Q$  and  $U$  components of the maximum likelihood band sky maps. From eqn. (3.4) we observe that the three terms:  $\delta \langle S_j \rangle$ ,  $\delta \langle S_j \cos 2\psi_j \rangle$ , and  $\delta \langle S_j \sin 2\psi_j \rangle$  can potentially induce a bias on the polarization Stokes parameters. The first term  $\delta \langle S_j \rangle$  has no impact if the maps of  $\langle \cos 2\psi \rangle$  and  $\langle \sin 2\psi \rangle$  vanish. This is the case in particular if detectors are arranged in sets of perfectly orthogonal pairs observing the sky along the same scanning path. If in addition for each such pair there is a matching pair observing at an angle of  $45^\circ$  relative to the first one, we get an optimized configuration [31] for which the  $3 \times 3$  matrix in eqn. (3.3) takes the form

$$\begin{pmatrix} 1 & 0 & 0 \\ 0 & \frac{1}{2} & 0 \\ 0 & 0 & \frac{1}{2} \end{pmatrix}^{-1}. \quad (3.5)$$

This simple form is preserved when observations are made with a set of such ‘optimized configurations’ oriented at any angle with respect to each other. This type of detector arrangement was used for the Planck mission, and is now standard for all proposed CMB polarization experiments. We then get

$$\begin{aligned} \delta \widehat{Q}_{BPM}(p) &= 2\delta \langle S_j \cos 2\psi_j \rangle, \\ \delta \widehat{U}_{BPM}(p) &= 2\delta \langle S_j \sin 2\psi_j \rangle, \end{aligned} \quad (3.6)$$

where under the sky model presented in Sect. 2

$$\begin{aligned}\delta \langle S_j \cos 2\psi_j \rangle &= \sum_{(c)} I_{(c)}(p) \sum_i \gamma_{(c),i} f_i(p) \langle \cos 2\psi_{i,j} \rangle, \\ \delta \langle S_j \sin 2\psi_j \rangle &= \sum_{(c)} I_{(c)}(p) \sum_i \gamma_{(c),i} f_i(p) \langle \sin 2\psi_{i,j} \rangle.\end{aligned}\quad (3.7)$$

Here the index  $(c)$  labels the non-CMB components of the sky model and  $i$  labels the detectors of the frequency channel under consideration (ideally supposed to have the same bandpass function). The coefficients  $\gamma_{(c),i}$  vary from detector to detector as a function of the stochastic realizations for the bandpass variation  $\delta\nu_{\min,i}$  and  $\delta\nu_{\max,i}$ .  $f_i(p)$  denotes the fraction of the total hits in pixel  $p$  from the detector  $i$ , and  $\langle \cos 2\psi_{i,j} \rangle$  and  $\langle \sin 2\psi_{i,j} \rangle$  are the components of the second-order crossing moments in pixel  $p$  for the detector  $i$ .

Before describing the predictions of the level of residual due to bandpass mismatch, we briefly digress to examine the properties of the crossing moment maps  $\langle \cos 2\psi \rangle$ ,  $\langle \cos 4\psi \rangle$ ,  $\langle \sin 2\psi \rangle$  and  $\langle \sin 4\psi \rangle$  for an individual detector for our model scanning pattern characterized by the parameter values:  $\alpha = 65^\circ$ ,  $\beta = 30^\circ$ ,  $\tau_{\text{spin}} = 10.002$  min, and  $\tau_{\text{prec}} = 96.2079$  min. Those maps, which are studied into more detail in Sect. 3.3, enter into the expression of the bandpass mismatch. In ecliptic coordinates, these quantities have a nearly symmetric pattern around the poles. Figure 2 shows the azimuthally averaged quantities (i.e., averaged over the ecliptic angle  $\phi$  or ecliptic longitude) as a function of the sine of the latitude of the maps. We observe that for a large fraction of pixels the spin-2 and spin-4 quantities (functions of period  $\pi$  and  $\pi/2$ , respectively) are less than 0.2.

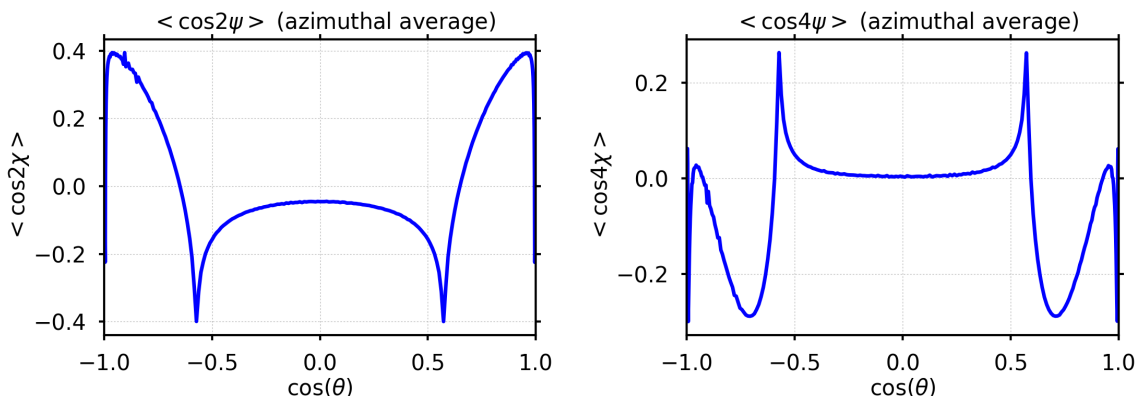


**Figure 2. Crossing moment map azimuthal averages.** We show the azimuthal average of  $\langle \cos 2\psi \rangle$  and  $\langle \cos 4\psi \rangle$  maps, constituting the totality of the component that is coherent on large angular scales. The corresponding  $\langle \sin 2\psi \rangle$  and  $\langle \sin 4\psi \rangle$  maps vanish for symmetry reasons.

### 3.1 Results

We now present numerical results for the bandpass mismatch maps and their power spectra based on simulations. We construct timestreams for each detector by reading a CMB map and a Galactic map, both at  $n_{\text{side}} = 256$ , which were preconvolved with a symmetric Gaussian beam of  $\theta_{\text{FWHM}} = 32'$ . We use an instrument model with actual locations of detectors in the focal plane as described in [13] or [11], depending on the case being considered. We note

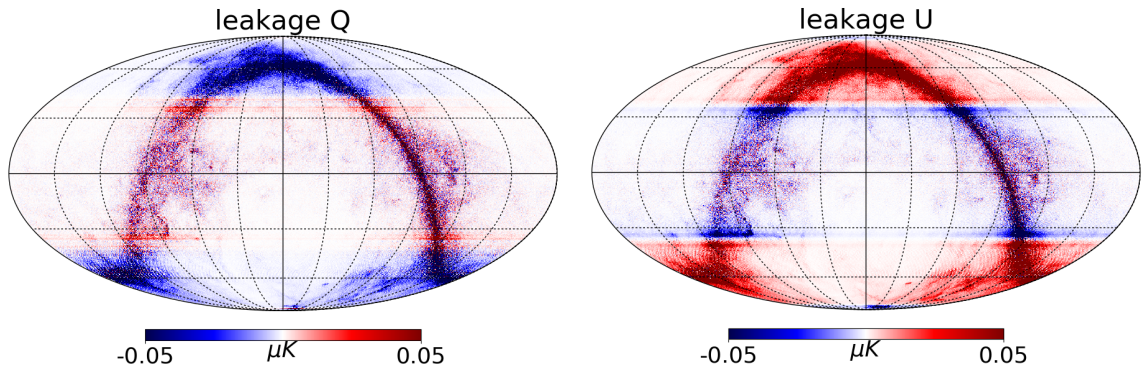


**Figure 3.**  $Q$  and  $U$  leakage maps, in ecliptic coordinates, with fiducial scanning parameters and  $N_{\text{det}} = 222$ .

however that the details of the arrangement of the detectors have little or no impact on the leakage power spectra. The Galactic map is rescaled from detector to detector using random errors in the bandpass generated as described in detail in Sect. 2. Then we construct combined  $I$ ,  $Q$ , and  $U$  maps obtained by applying the map making equation as given in eqn. (3.1). No noise is included in the simulation, because the map making method is linear and the noise does not affect the bias induced by the mismatch. For the same reason we do not introduce sky emission polarization in simulations. The bandpass mismatch properties of each detector are generated randomly and in a statistically independent manner. Figure 3 shows the  $Q$  and  $U$  leakage maps:  $\delta Q_{\text{BPM}}$  and  $\delta U_{\text{BPM}}$  for one particular realization. The output polarization maps result from optimal map making using our simulated noiseless and polarizationless timestreams for the 140 GHz channel and are shown in ecliptic coordinates. The simulation assumed 222 detectors, which is the number of detectors composing the LiteBIRD arrays described in [13], spread over a large focal plane approximately 10 degrees wide observing with no HWP. The detector polarizer covers the full range of angles in the focal plane with 22.5 degree separation. We assume the fiducial scanning parameters  $\alpha = 65^\circ$ ,  $\beta = 30^\circ$ ,  $\tau_{\text{spin}} = 10$  min, and  $\tau_{\text{prec}} = 96.1803$  min for the center of the focal plane (see Section 3.3 for a discussion of the choice of  $\tau_{\text{spin}}$  and  $\tau_{\text{prec}}$  to minimize the inhomogeneity of the scanning pattern which is responsible for Moiré effects in the crossing moment maps). At 140 GHz the bandpass mismatch error in polarization is dominated by the  $I$  component of the thermal dust emission, although there are subdominant contributions from the diffuse Galactic synchrotron emission and other non-primordial (non-CMB) components. The length of the survey in this simulation is exactly one sidereal year in order to ensure as uniform and complete sky coverage as possible and hence facilitate the interpretation of those results. We observe that the leakage is concentrated near the Galactic plane, as expected. The bands at equal latitude visible in the leakage maps correspond to regions where the second order crossing moments depart significantly from zero (Fig. 2), and as can be seen from eqn. (3.7), there is a strong correlation between the relative leakage amplitude and these moments.

Figures 4, 5 and 6 show the bandpass mismatch leakage contributions to the  $EE$  and  $BB$  power spectra in different observing configurations. The power spectra are computed after the 20% of the sky where the thermal dust emission is strongest is masked. The data in this masked region is set to zero with no apodization (which is unnecessary since the small-scale power in the leakage maps dominates over the spurious power induced by the masking). For

comparison we also show the CMB B- mode spectrum for two different values of  $r$ . The dashed curves show how the signal is attenuated by beam smearing assuming the 140 GHz FWHM beamwidth of  $32'$  fitted to a Gaussian profile for the present LiteBIRD configuration [32]. As will be demonstrated later, neglecting the discreteness of the scans, the overall amplitude of the leakage due to bandpass mismatch is nearly Gaussian and of zero mean, and the variations of  $\gamma_{dust}$  impact all multipoles of the leakage map power spectrum in a correlated way. For this reason, an accurate estimate of the average leakage power spectrum requires averaging many independent realizations even if many detectors are used for the simulations. At least on large angular scales, the fluctuations in the power spectrum due to different realizations is roughly an overall amplitude varying as the square of a Gaussian.

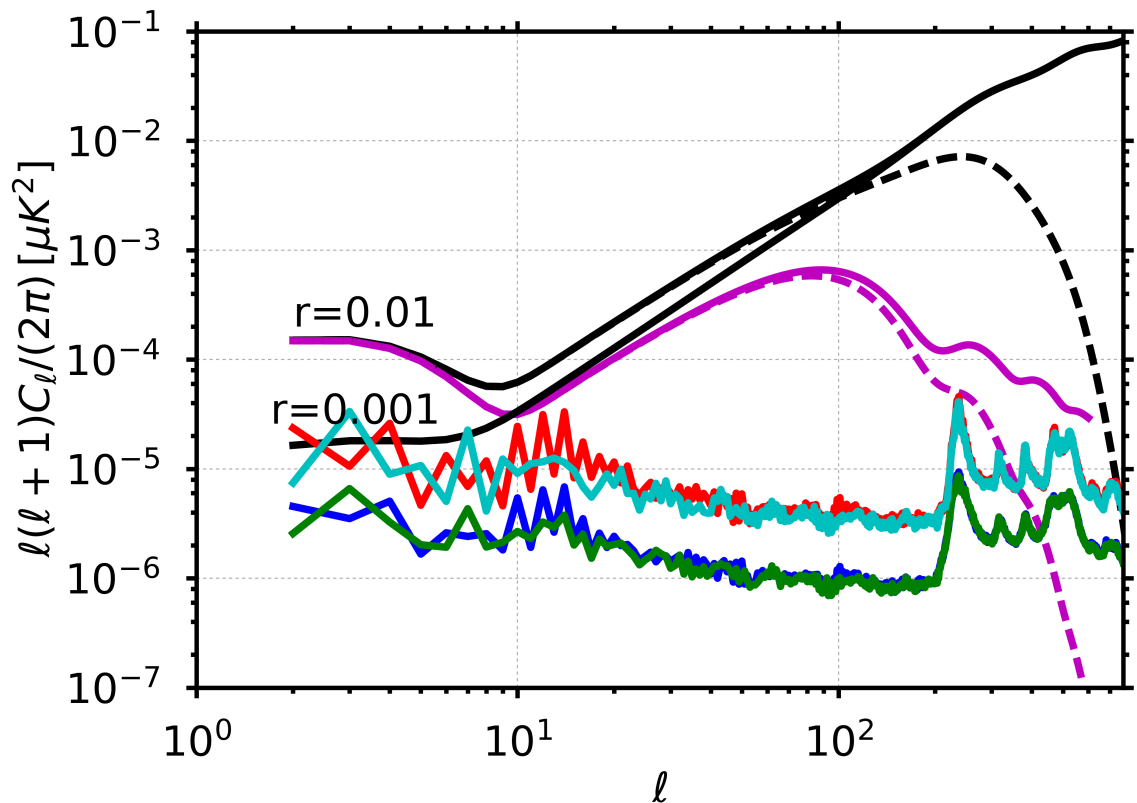
We find that with all other parameters equal, the bandpass mismatch error amplitude scales as  $1/\sqrt{N_{\text{det}}}$  where  $N_{\text{det}}$  is the number of detectors (and hence the power spectrum scales as  $1/N_{\text{det}}$ ). This scaling becomes more accurate when  $N_{\text{det}}$  becomes large, as shown by comparing the  $EE$  and  $BB$  leakage power spectra for  $\tau_{\text{spin}} = 10$  min,  $\tau_{\text{prec}} = 96.1803$  min and  $N_{\text{det}}$  of either 74 or 222. The pairs of spectra have the same shape but the ratio of power spectrum amplitudes is consistent with the predicted ratio  $222/74 = 3$ .

Figure 5 shows the  $BB$  power spectra for  $\alpha = 65^\circ$ ,  $\beta = 30^\circ$  for several spin and precession period combinations. We see that the characteristics of the leakage power spectrum (and in particular the location of the peaks at  $\ell \leq 100$ ), depend on the exact values of  $\tau_{\text{spin}}$  and  $\tau_{\text{prec}}$ . A proper value of the ratio  $\tau_{\text{prec}}/\tau_{\text{spin}}$  moves the peaks in the bandpass leakage spectrum to higher  $\ell$ , away from the location of the maximum of the primordial B-mode recombination bump.

Figure 6 compares the  $BB$  power spectra for different opening angles  $\alpha$  and  $\beta$ , and also different scan rates. With the constraint  $\alpha + \beta = 95^\circ$ , scan strategies with larger precession angle produce less leakage because they allow for more homogeneous scan angle coverage per pixel, and hence lower  $|\langle \cos 2\psi_j \rangle|$  and  $|\langle \sin 2\psi_j \rangle|$  per individual detector.

We observe that the power spectra above (without a HWP) are approximately proportional to  $\ell^{-\eta}$  where  $\eta \approx 2.5$ . This angular power spectrum is less steep than that of dust emission itself. The shape of the resulting leakage spectrum can be expressed as a kind of convolution between the harmonic coefficients of the crossing moment maps and of the dust component map (see Ref. [33] for an analytical explanation of this power law). This spectral shape is problematic on very large scales, for example near the reionization bump, because the ratio of the bandpass mismatch to the white noise component of the detector noise (having an  $\eta \approx 0$  spectrum) increases toward lower multipole number  $\ell$ . We observe some dependence of the amplitude of the leakage spectra with respect to the scanning strategy parameters  $\alpha$  and  $\beta$ . Scanning strategies with more uniform angular coverage (provided by larger precession angles for the studied cases) have a lower leakage amplitude.

When the experiment observes with a rotating HWP, the equivalent of an optimized polarimeter configuration is straightforwardly obtained when the HWP observes a given sky position  $\hat{p}$  during an integer number of turns (and, thus, for an evenly spread set of angles between 0 and  $2\pi$ ). In practice however, the pointing direction moves while the HWP rotates, and hence data samples are not usually so evenly distributed. However, when the HWP rotates at 1.467 Hz (88 rpm) while the instrument beam scans the sky with a spin period of  $\tau_{\text{spin}} = 10$  minutes and with a  $30^\circ$  angle, the beam is displaced by  $0.204^\circ$  (about  $12.3'$ ) each time the HWP makes one turn. Neglecting this displacement, single detector timelines of  $I$ ,  $Q$ , and  $U$  with no bandpass mismatch leakage can be straightforwardly obtained from the data set, and projected onto sky maps with optimal noise averaging, i.e., equivalent to



**Figure 4.**  $EE$  and  $BB$  leakage power spectra for  $\alpha = 65^\circ$ ,  $\beta = 30^\circ$ ,  $\tau_{\text{spin}} = 10$  min,  $\tau_{\text{prec}} = 96.1803$  min, and combining data for either 74 or 222 detectors. The red curve corresponds to  $BB$  with 74 detectors, the cyan to  $EE$  with 74 detectors, the blue to  $BB$  with 222 detectors and the green to  $EE$  with 222 detectors. The purple curve represents a model of primordial  $B$  mode power spectrum with fiducial cosmological parameters after Planck for  $r = 0.01$ , the black curves are including lensing for  $r = 0.01$  and  $r = 0.001$ . The dashed curves show the effect of convolving with a 32 arcmin beam. This plot demonstrates the  $1/N_{\text{det}}$  dependence of the level of the power spectra.

the generalized least square solution of eqn. (3.1). Of course, a real-life HWP is not perfectly achromatic and hence is likely to introduce bandpass mismatch effects of its own. We postpone to future work the study of this type of effect.

To illustrate the added value of a perfect HWP, we perform a simple set of simulations in which the input sky (smoothed by a 32' beam) is a Healpix map pixelized at  $n_{\text{side}} = 256$ . The pixel size is well matched to the rotation speed of the HWP, which makes about one turn while it crosses a pixel. However, numerical effects will generate unevenness in the angular coverage of each pixel, and thus, when multi-detector maps are made using eqn. (3.1), small bandpass leakage mismatch effects will subsist. Simulating the observation of this model sky with the use of a HWP spinning at 88 rpm and other parameters set to  $\alpha = 65^\circ$ ,  $\beta = 30^\circ$ ,  $\tau_{\text{spin}} = 10$  min,  $\tau_{\text{prec}} = 96.1803$  min, we obtain the small residual leakage shown in Fig. 7, which confirms the effectiveness of the HWP in reducing bandpass leakage by homogenizing the angular coverage in each pixel. The shape of the spectrum of the residual is similar to that of white noise. Its origin is in the small unevenness of the angle distributions across the pixels and is an artefact of sky pixelization.

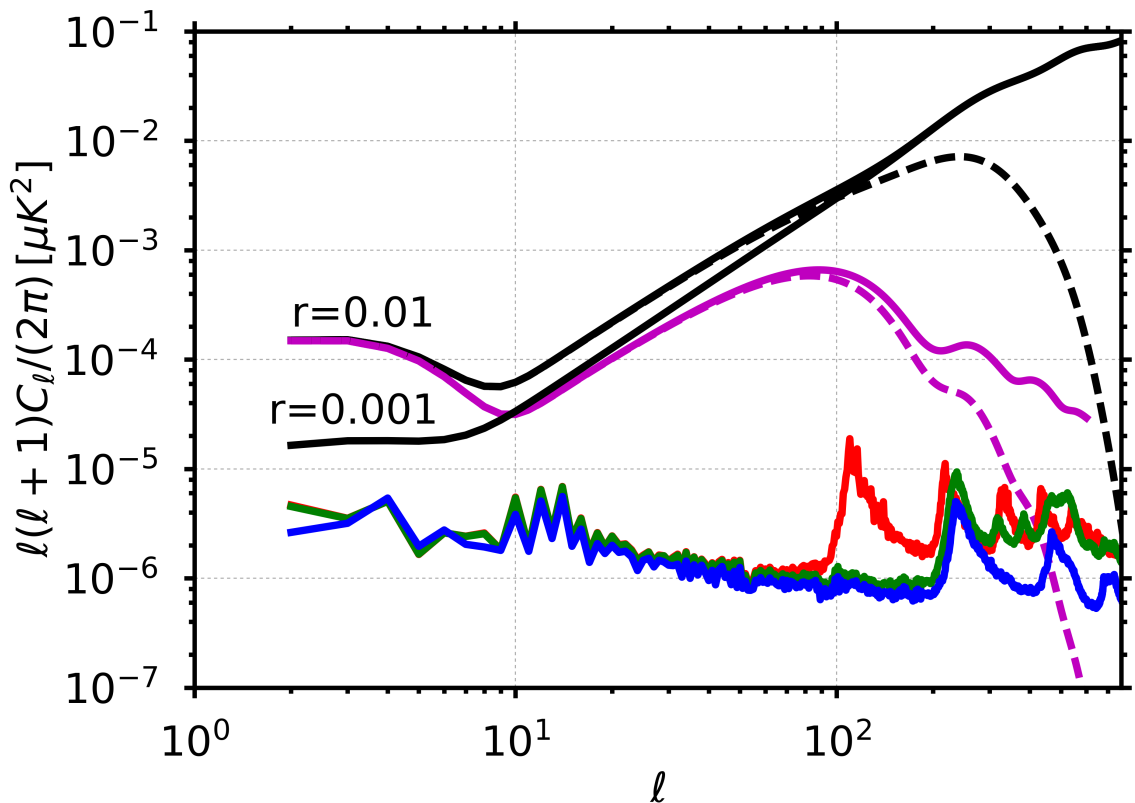


**Figure 5.** *BB* leakage power spectra for  $\alpha = 65^\circ$ ,  $\beta = 30^\circ$ ,  $\tau_{\text{spin}}=10$  min,  $\tau_{\text{prec}}=93$  min (red);  $\tau_{\text{spin}}=10$  min,  $\tau_{\text{prec}}=96.1803$  min (green); and  $\tau_{\text{spin}}=10/3$  min,  $\tau_{\text{prec}}=96.1803$  min (blue). Simulations include 222 detectors and 365 days observation. See the Fig. 4 caption for a description of the model curves.

We verify that in case of a perfect HWP, the multi-detector solution for the polarization is close to the solution consisting in combining single detector (including the HWP) polarization maps, as the residual leakage and its impact of  $r$  that can be read off the plot, is negligible.

	$2 \leq \ell \leq 10$	$10 \leq \ell \leq 200$
$\alpha = 30^\circ; \beta = 65^\circ; \tau_{\text{prec}} = 4$ days; $\omega_{\text{spin}} = 0.5$ rpm	$1.83 \times 10^{-3}$	$9.32 \times 10^{-5}$
$\alpha = 50^\circ; \beta = 45^\circ; \tau_{\text{prec}} = 4$ days; $\omega_{\text{spin}} = 0.5$ rpm	$6.49 \times 10^{-4}$	$4.66 \times 10^{-5}$
$\alpha = 50^\circ; \beta = 45^\circ; \tau_{\text{prec}} = 96$ min; $\omega_{\text{spin}} = 0.1$ rpm	$6.32 \times 10^{-4}$	$3.08 \times 10^{-5}$
$\alpha = 65^\circ; \beta = 30^\circ; \tau_{\text{prec}} = 93$ min; $\omega_{\text{spin}} = 0.1$ rpm	$3.29 \times 10^{-4}$	$7.61 \times 10^{-5}$
$\alpha = 65^\circ; \beta = 30^\circ; \tau_{\text{prec}} = 96$ min; $\omega_{\text{spin}} = 0.1$ rpm	$3.27 \times 10^{-4}$	$2.11 \times 10^{-5}$
$\alpha = 65^\circ; \beta = 30^\circ; \tau_{\text{prec}} = 96$ min; $\omega_{\text{spin}} = 0.3$ rpm	$3.03 \times 10^{-4}$	$1.77 \times 10^{-5}$

**Table 1.** Contribution of bandpass mismatch error to the tensor-to-scalar ratio  $r$  computed according to eqn. (3.8). The level of the bandpass leakage relative to primordial B-mode signals is acceptable at the angular scale of the recombination bump, but problematic in the reionization bump at  $\ell \leq 10$ . Scanning strategies with larger  $\alpha$  and smaller  $\beta$  perform better, as they provide more uniform angular coverage in each pixel.

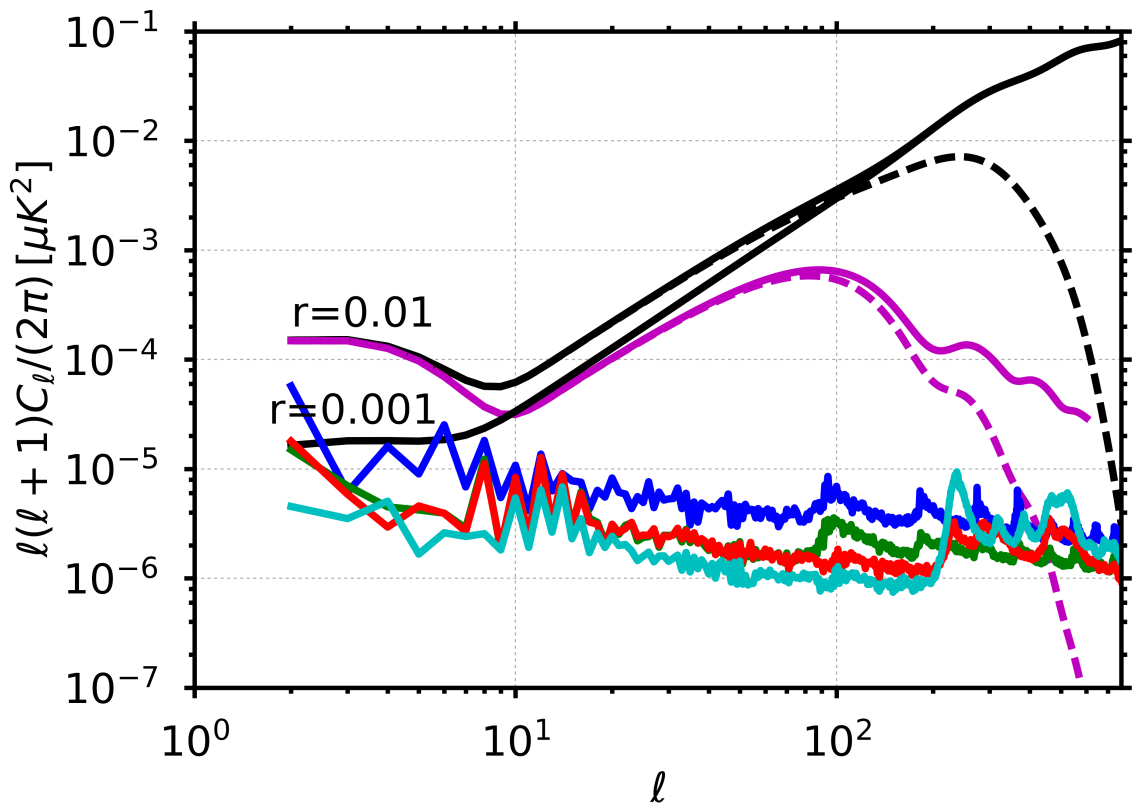


**Figure 6.**  $BB$  leakage power spectra for different scanning parameters. In cyan:  $\alpha = 65^\circ, \beta = 30^\circ, \tau_{\text{spin}}=10 \text{ min}, \tau_{\text{prec}}=96.1803 \text{ min}$ , red:  $\alpha = 50^\circ, \beta = 45^\circ, \tau_{\text{spin}}=10 \text{ min}, \tau_{\text{prec}}=96.1803 \text{ min}$ , green:  $\alpha = 50^\circ, \beta = 45^\circ, \tau_{\text{spin}}=2 \text{ min}, \tau_{\text{prec}}=4 \text{ day}$ , blue:  $\alpha = 30^\circ, \beta = 65^\circ, \tau_{\text{spin}}=2 \text{ min}, \tau_{\text{prec}}=4 \text{ day}$ . Spectra are computed for 222 detectors. Curves for the  $B$  mode model are described in Fig. 4 caption. For the scanning strategies with a long precession period, we computed spectra for 100 detectors rescaling to 222 equivalent detectors using the  $1/N_{\text{det}}$  dependence.

Table 1 shows the contribution to  $r$  that would result from uncorrected bandpass mismatch based on its power spectrum averaged over many realizations, calculated using the projection

$$\hat{\delta r} = \frac{\sum_{\ell=\ell_{\text{min}}}^{\ell_{\text{max}}} (2\ell+1)C_\ell \hat{C}_\ell}{\sum_{\ell=\ell_{\text{min}}}^{\ell_{\text{max}}} (2\ell+1)C_\ell^2}. \quad (3.8)$$

Here  $C_\ell$  is the power spectrum for the primordial  $B$  mode signal normalized to  $r = 1$ . The Table shows  $\delta r$  calculated for two ranges of  $\ell$ : one with  $\ell \in [2, 10]$  to isolate the signal from the re-ionization bump, and another with  $\ell \in [10, 100]$  to isolate the signal arising from the recombination bump. The results in the table assume  $N_{\text{det}} = 222$  detectors, but can be rescaled based on the  $1/N_{\text{det}}$  dependence to other numbers of detectors. These results are only an order of magnitude estimate because they are based on a single 140 GHz channel, and it has been assumed that very low and very high frequency channels have been used to removed the non-primordial components completely. We stress that the bandpass mismatch power spectrum is not a simple bias that can be predicted and subtracted away because its overall amplitude suffers large fluctuations, which is of the same order of magnitude as the

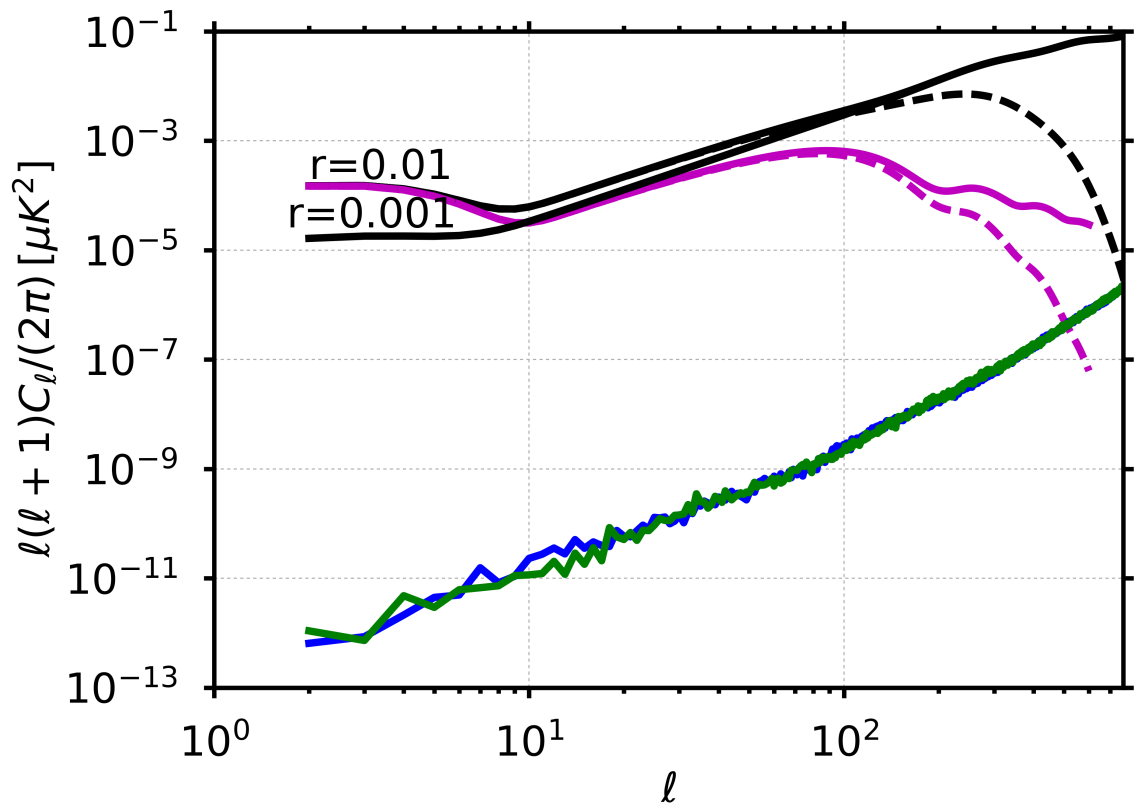


**Figure 7.** *EE* and *BB* leakage power spectra with rotating HWP for  $\alpha = 65^\circ$ ,  $\beta = 30^\circ$  and spin period of 10 min with a HWP rotating at 88 rpm for 50 detectors.

average bias itself.

### 3.2 Analytic estimates

With the objective of finding fast and easy ways to predict the magnitude of potential leakage without running many Monte Carlo simulations, and in order to understand how the patterns shown in the leakage map in Fig. 3 are related to the scanning strategy, we now study theoretically in more detail how the leakage manifests itself in the polarization maps. To this effect, we expand the solution of the map making equation [eqn. (3.1)].

We derive a simple expression for the leakage originating from differencing the signal from a pair of orthogonally polarized detectors observing instantaneously at the same location in the sky, so that data of the two detectors of the pair  $i$  at time  $t$  in pixel  $p$  denoted as  $S_{i;a}(t)$  and  $S_{i;b}(t)$  are given by

$$\begin{aligned} S_{i;a}(t) &= I_{i;p} + Q_p \cos 2\psi(t) + U_p \sin 2\psi(t) + M_{i;p}, \\ S_{i;b}(t) &= I_{i;p} - Q_p \cos 2\psi(t) - U_p \sin 2\psi(t) - M_{i;p}. \end{aligned} \quad (3.9)$$

Here we assume no noise and perfect calibration on the CMB (e.g., using the CMB dipole), and  $\psi$  is the polarizer angle for detector  $a$ .  $I_{i;p}$ ,  $Q_p$ ,  $U_p$  are the Stokes parameters of the sky signal,  $I_{i;p}$  being the mean intensity parameter for the detector pair  $i$ , and  $M_{i;p}$  represents



the bandpass mismatch component, which is given by

$$M_{i;p} = \frac{1}{2} \sum_{(c)} \left( \gamma_{(c)}^a - \gamma_{(c)}^b \right) I_{p,(c)}. \quad (3.10)$$

Here the index  $(c)$  labels the non-CMB sky components. The coefficient differences  $(\gamma_{(c)}^a - \gamma_{(c)}^b)$  vary from detector pair to detector pair, as explained in Sect. 2 (see in particular eqn. (2.3)). To minimize clutter, we have suppressed the index  $i$  labelling the detector pairs. We neglect the subdominant effect of bandpass mismatch on the polarized sky components. As in the previous Section, we neglect noise in our analysis. The estimated noiseless Stokes parameter maps  $\widehat{Q}_p$  and  $\widehat{U}_p$  can be expanded as  $\widehat{Q}_p = Q_p + \delta Q_p$  and  $\widehat{U}_p = U_p + \delta U_p$ , where  $\delta Q$  and  $\delta U$  represent the leakages to polarization resulting from bandpass mismatch. Ideal solutions with no leakage are given in eqn. (3.9).

The map making equation gives

$$\begin{pmatrix} \widehat{I}_p \\ \widehat{Q}_p \\ \widehat{U}_p \end{pmatrix} = \begin{pmatrix} 1 & 0 & 0 \\ 0 & \frac{1}{2}(1 + \langle \cos 4\psi \rangle) & \frac{1}{2}\langle \sin 4\psi \rangle \\ 0 & \frac{1}{2}\langle \sin 4\psi \rangle & \frac{1}{2}(1 - \langle \cos 4\psi \rangle) \end{pmatrix}^{-1} \begin{pmatrix} \langle S \rangle \\ \langle \frac{1}{2}(S_a - S_b) \cos 2\psi \rangle \\ \langle \frac{1}{2}(S_a - S_b) \sin 2\psi \rangle \end{pmatrix}, \quad (3.11)$$

and the zeros in the 3x3 matrix result because the exact orthogonality of the two detectors of each pair insures that  $\langle \cos 2\psi \rangle$  and  $\langle \sin 2\psi \rangle$  vanish exactly [compare with eqn. (3.4)], so that the expression for  $\widehat{I}_p$  decouples from the expressions for  $\widehat{Q}_p$  and  $\widehat{U}_p$ . Consequently, the leakages are given by

$$\begin{aligned} \begin{pmatrix} \delta Q_p \\ \delta U_p \end{pmatrix} &= \begin{pmatrix} \frac{1}{2}(1 + \langle \cos 4\psi \rangle) & \frac{1}{2}\langle \sin 4\psi \rangle \\ \frac{1}{2}\langle \sin 4\psi \rangle & \frac{1}{2}(1 - \langle \cos 4\psi \rangle) \end{pmatrix}^{-1} \begin{pmatrix} \langle M_p \cos 2\psi \rangle \\ \langle M_p \sin 2\psi \rangle \end{pmatrix} \\ &= \frac{2}{(1 - \langle \cos 4\psi \rangle)^2 - \langle \sin 4\psi \rangle^2} \begin{pmatrix} 1 + \langle \cos 4\psi \rangle & -\langle \sin 4\psi \rangle \\ -\langle \sin 4\psi \rangle & 1 - \langle \cos 4\psi \rangle \end{pmatrix} \begin{pmatrix} \langle M_p \cos 2\psi \rangle \\ \langle M_p \sin 2\psi \rangle \end{pmatrix}. \end{aligned} \quad (3.12)$$

Assuming that  $\langle \cos 4\psi \rangle^2 + \langle \sin 4\psi \rangle^2 \ll 1$  (which is not so bad an approximation except very near the poles), we obtain

$$\begin{pmatrix} \delta Q_p \\ \delta U_p \end{pmatrix} \approx 2 \begin{pmatrix} \langle M_p \cos 2\psi \rangle \\ \langle M_p \sin 2\psi \rangle \end{pmatrix}. \quad (3.13)$$

For one Galactic component, by replacing  $M_p$  by its expression in eqn. (3.10), the relative amplitude of the leakage can be written as

$$\begin{pmatrix} \delta Q_p \\ \delta U_p \end{pmatrix} \frac{I_{\text{Gal};p}}{I_{\text{Gal};p}} = \left( \gamma_{\text{Gal}}^a - \gamma_{\text{Gal}}^b \right) \begin{pmatrix} \langle \cos 2\psi \rangle \\ \langle \sin 2\psi \rangle \end{pmatrix}. \quad (3.14)$$

The term on the right hand side is one of the crossing moment terms for a single detector. We should then observe a large correlation between the two maps on the two sides of the equation. We have verified, with the help of simulations of data for one detector pair, this relationship for two different scanning strategies:  $\alpha = 65^\circ$  and  $\beta = 30^\circ$  and  $\alpha = 50^\circ$  and  $\beta = 45^\circ$ . Figure 8 shows the relative leakage map  $\delta Q_p/I_{\text{Gal};p}$  and the quantity  $\sum \cos 2\psi/n_p$ . The  $U$  component (not shown here) exhibits similar properties.

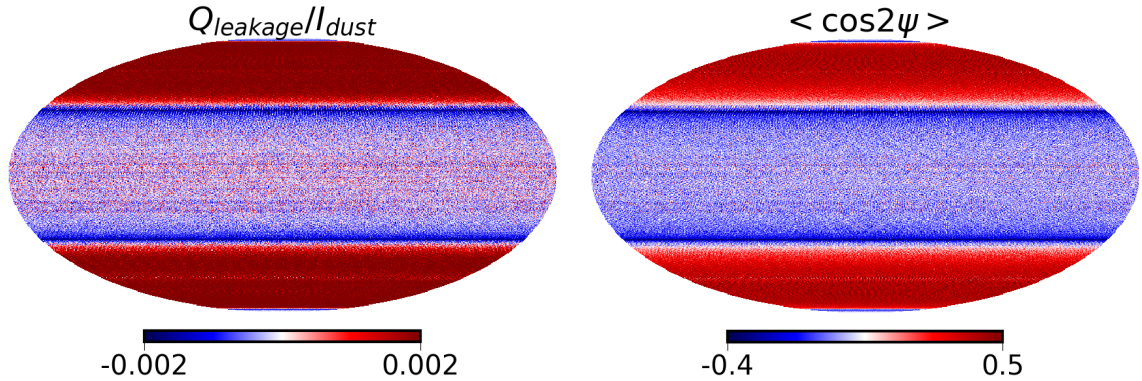


**Figure 8.** Left: Leakage for the  $Q$  component relative to the dust temperature ( $\delta Q/I_{\text{Gal}}$ ) after polarization reconstruction using one bolometer pair only and a one year observation time. Right: Averaged  $\cos 2\psi$  in each pixel for one bolometer after one year observation time. This quantity is strongly correlated to the relative leakage  $Q$  component with respect to the dust intensity.

Figure 9 shows the correlation of the two maps, by plotting the values of one map versus the other for a subset of pixels. We observe a high correlation between the two maps. We verify that the slope is given by the coefficient  $\Delta\gamma = \gamma_a - \gamma_b$  as derived in eqn. (3.14). This figure shows the tight link between the crossing moments and the relative leakage due to bandpass mismatch. It also shows that the approximations made to derive eqn. (3.14) are valid since we observe a relatively small scatter around the linear slope. The outliers in the Figure are due to pixels near the ecliptic poles where the angle coverage is less uniform for the scanning parameters used as a baseline in this work.

We now consider the solution combining more detectors. The generalization of eqn. (3.13) gives for the resulting leakage component

$$\begin{pmatrix} \delta Q_p \\ \delta U_p \end{pmatrix} = \begin{pmatrix} \frac{1}{2} \sum_i \sum_j (1 + \cos 4\psi_i^j) & \frac{1}{2} \sum_i \sum_j \sin 4\psi_i^j \\ \frac{1}{2} \sum_i \sum_j \sin 4\psi_i^j & \frac{1}{2} \sum_i \sum_j (1 - \cos 4\psi_i^j) \end{pmatrix}^{-1} \begin{pmatrix} \sum_i \sum_j \cos 2\psi_i^j M_{i,p} \\ \sum_i \sum_j \sin 2\psi_i^j M_{i,p} \end{pmatrix} \quad (3.15)$$

where we sum over all the detector pairs indexed by  $i$  and over all samples  $j$  falling in pixel  $p$  for each detector. In this case, for which we consider the realistic configuration of more than one pair of detectors per pixel, the covariance matrix above becomes nearly diagonal. As the number of detectors is increased, the matrix in eqn. (3.15) becomes increasingly diagonal. The total leakage is then simply, replacing the leakage term  $M_p$  by its expression:

$$\frac{\delta Q_p}{I_{\text{Gal};p}} \approx \frac{2}{N_{\text{hit}}} \sum_i \Delta\gamma_i \sum_j \cos 2\psi_i^j, \quad (3.16)$$

using eqn. (3.10), where we have defined  $N_{\text{hit}}$  as the total number of hits including all detectors (and not only count 1 per detector pair which explains the cancellation of the  $1/2$  factors since the sum runs over detector pairs), and  $\Delta\gamma_i = \gamma_i^a - \gamma_i^b$ . The leakage vanishes if each individual detector has uniform angle coverage. We observe that the relevant quantities to estimate the level of leakage for a given scanning strategy are the individual detector second order crossing moments. Following our hypothesis that the  $\gamma$  parameters are random and uncorrelated, we

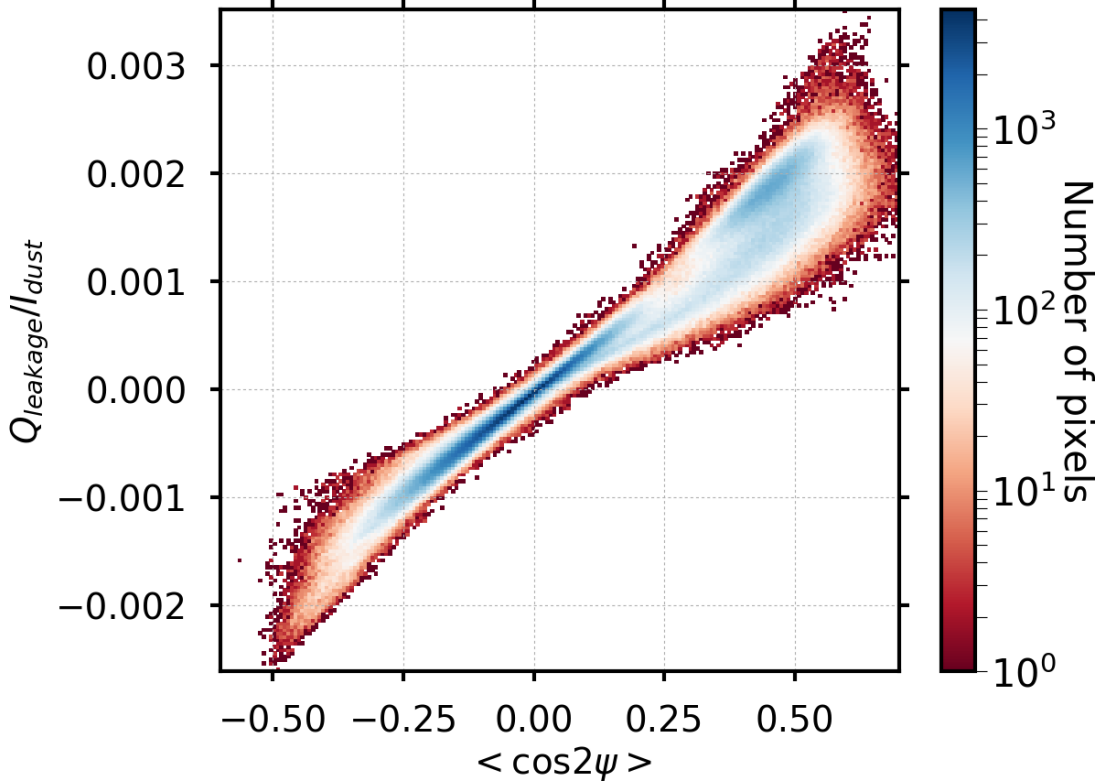


**Figure 9.** Values of the relative leakage  $\delta Q_p/I_{\text{Gal};p}$  for a pair of detectors with orthogonal polarizations of a function of the scanning strategy parameter  $(1/n_p) \sum \cos 2\psi$  (see text) after map making with two detectors only. We observe a tight correlation between the relative leakage and the second order crossing moments.

express the variance of the leakage map as:

$$\text{Var} \left( \frac{\delta Q_p}{I_{\text{Gal};p}} \right) \approx \sum_i \text{Var}(\Delta\gamma_i) \left( \sum_j \cos 2\psi_i^j \right)^2 \left( \frac{2}{N_{\text{hit}}} \right)^2, \quad (3.17)$$

which gives, since  $\text{Var}(\Delta\gamma) = 2\text{Var}(\gamma)$ :

$$\text{Var} \left( \frac{\delta Q_p}{I_{\text{Gal};p}} \right) \approx 4 \frac{\text{Var}(\gamma)}{N_{\text{det}}} \left\langle \left( \frac{\sum \cos 2\psi_i^j}{\bar{n}_p} \right)^2 \right\rangle_{\text{det}}, \quad (3.18)$$

where  $\langle \cdot \rangle_{\text{det}}$  denotes average over all detectors, and  $\bar{n}_p = \frac{N_{\text{hit}}}{N_{\text{det}}}$  is the average number of hits per detector. The expression for the  $U$  component is similar with the cosine replaced by a sine. This expression of the variance of the leakage map is also valid if detectors are not arranged by pairs.

Figure 10 compares the maps of the variance on the left-hand side of the previous relationship which was estimated with ten independent realizations of the bandpass parameters, with the quantity  $\left\langle \left( (1/\bar{n}_p) \sum \cos 2\psi_i \right)^2 \right\rangle_{\text{det}}$ . Figure 11 shows the correlations between the

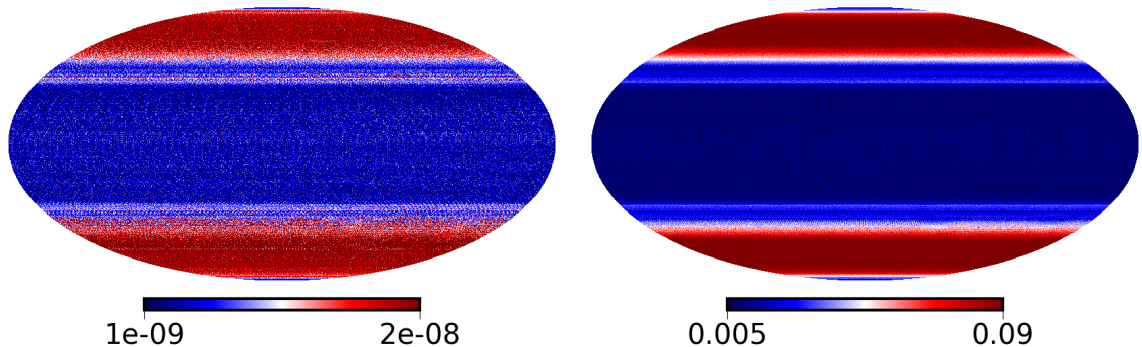


**Figure 10.** Left: Estimated leakage variance of the  $Q$  component relative to the dust temperature ( $\text{Var}(\delta Q_p/I_{\text{Gal};p})$ ) after polarization reconstruction using all bolometer pairs and one year of observations. We used 10 independent realizations of the bandpass to estimate the variance. Right: Averaged  $\left\langle \left( (1/\bar{n}_p) \sum \cos 2\psi_i^d \right)^2 \right\rangle_{\text{det}}$  in each pixel for all bolometers after one year observation time. As for the detector pair case, we observe a tight correlation of the two maps on large angular scales

two quantities on a scatter plot. We observe a significant correlation of the two quantities, especially on large scales. The dispersion is partly due to the limited number of realizations to estimate the variance. Nevertheless, this shows that the level of leakage can be evaluated by estimating the second order crossing moments only for different scanning strategies without the need of running large simulations. This result explains what was observed in Fig. 6, showing the level of the leakage with respect to the scanning parameters  $\alpha$  and  $\beta$ . The strategies with more uniform angle distribution (the ones with larger precession angle) show lower residuals (see also [34] for the link with other systematic effects).

Results show that contamination from bandpass mismatch even if small could contribute to the  $B$  mode spectrum at a non-negligible level, close to the detection limit of primordial  $B$  modes with future satellite missions. Systematic variation of the bandpass functions across the focal plane, as opposed to the uncorrelated random variations assumed in this study, could produce larger errors. These considerations motivate developing correction methods, which we present in the companion paper [19].

### 3.3 Importance of avoiding resonances

Here we briefly explain some considerations for choosing the scan frequency parameters  $\omega_{\text{spin}}$  and  $\omega_{\text{prec}}$ . We found that to obtain good crossing moment maps, careful attention must be paid to choosing the ratios of the hierarchy of scan frequencies  $\omega_{\text{ann}} \ll \omega_{\text{prec}} \ll \omega_{\text{spin}}$ , and when there is a continuously rotating HWP also  $\omega_{\text{HWP}}$ . For  $\omega_{\text{prec}}/\omega_{\text{ann}}$ , we choose to make this number an integer so that the scan pattern closes. In all the simulations reported here, we assumed a single survey of exactly one year in duration. Given the large number of precession cycles in a year, this requirement can be achieved by means of a very small adjustment in  $\omega_{\text{prec}}$ . One might also want to do the same for the spin period, but this is less critical because of its shortness compared to a year.

More critical is the ratio  $\theta = \omega_{\text{spin}}/\omega_{\text{prec}}$ , which must be chosen so that  $\theta$  cannot be well approximated by simple fractions of the form  $p/q$  where  $p$  and  $q$  are relatively prime and  $q$  is small in a sense that we shall make more precise shortly. Of concern are exact or near exact resonances where  $q$  is less than of order  $\omega_{\text{prec}}/\omega_{\text{spin}}$ .

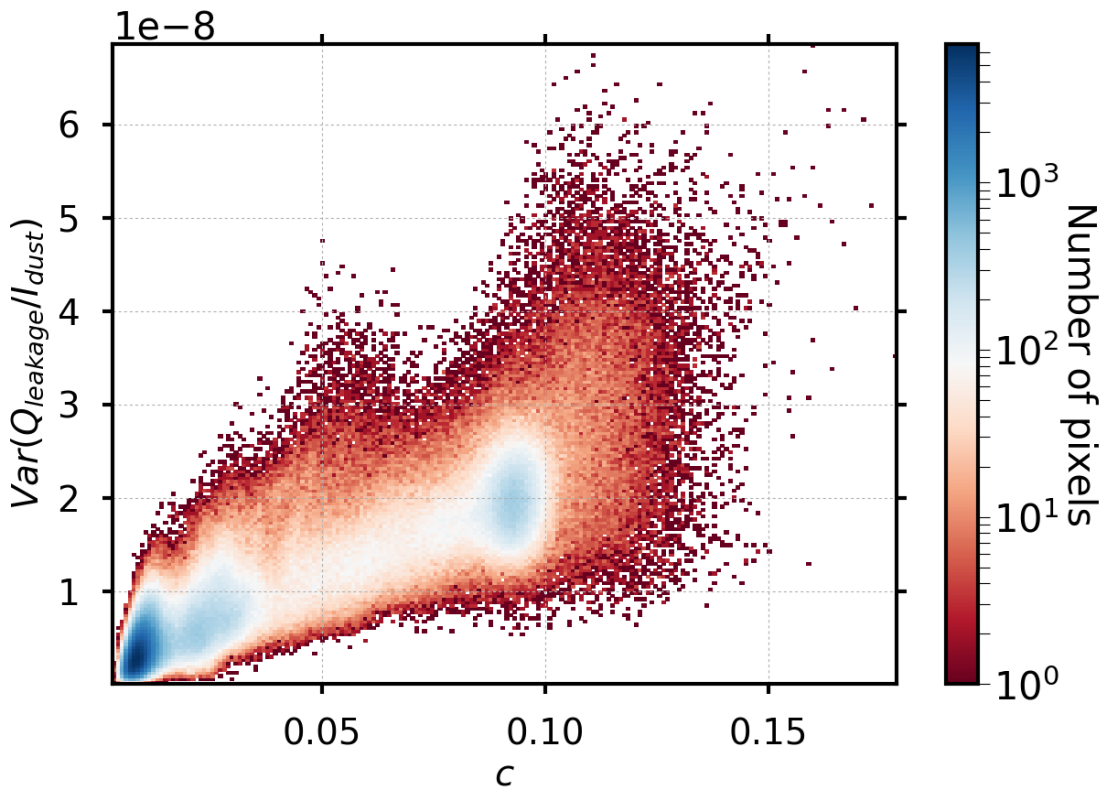


**Figure 11.** Estimated variance distribution of the relative leakage parameter:  $\text{Var}(\delta Q_p/I_{\text{Gal},p})$  as a function of  $c = \left\langle \left( (1/\bar{n}_p) \sum \cos 2\psi_{t,i} \right)^2 \right\rangle_{\text{det}}$  (see text) after map making including all detectors. We have averaged over ten realizations to estimate the variance.

Before entering into the theory of how the ratio  $\theta$  should be chosen (and jumping ahead slightly), we show what goes wrong when  $\theta$  is not well chosen. For example, our first try had  $\tau_{\text{spin}} = 10$  min and  $\tau_{\text{prec}} = 93$  min and gave hit count and crossing moment maps with clearly visible Moiré patterns at intermediate angular scales, as shown in Fig. 12, showing clear evidence of a near resonance. However, when  $\omega_{\text{prec}}$  was sped up by the Golden ratio  $\Phi = (1 + \sqrt{5})/2 = 1.61803398875$  (reputed to be the “most irrational” number),<sup>3</sup> these undesirable Moiré patterns disappear, as shown in the bottom right panel of the Figure. The same effect could be achieved by altering the ratio  $\theta$  by just 5%, so that the spin cycle has the same phase as with the Golden ratio sped up. We note that the effect of these Moiré patterns on the bandpass mismatch power spectra is to introduce peaks at multipole numbers at which the bandpass mismatch error is increased by up to about an order of magnitude beyond the baseline, where it would be if  $\theta$  had been well chosen to avoid near resonances. We also note that when a continuously rotating HWP is introduced, there are two independent ratios to worry about, although the artefacts are less acute than in the case of no rotating HWP.

<sup>3</sup>See for example Michael Berry, (1978, September), *Regular and irregular motion*, in S. Jorna (Ed.), AIP Conference proceedings (Vol. 46, No. 1, 16-120), AIP for a nice discussion of these questions in a different context, that of perturbations of integrable systems in classical mechanics, KAM theory, and the stability of the solar system.

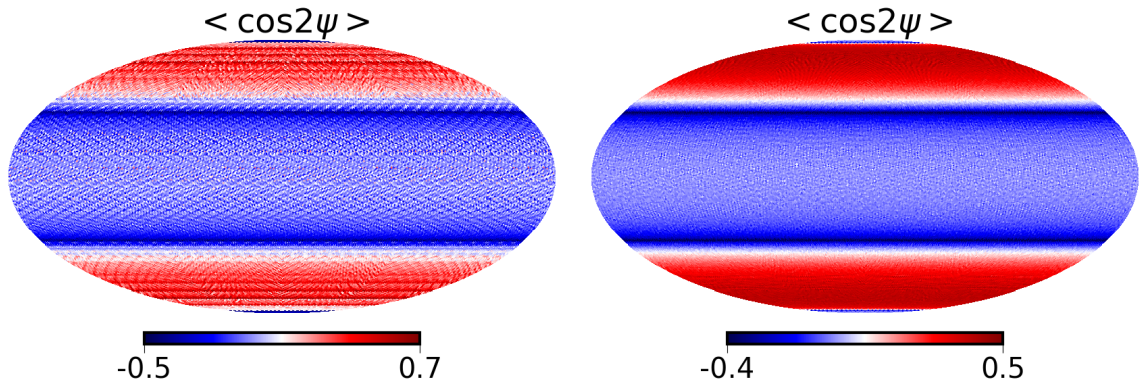


**Figure 12. Effect of a poorly chosen scanning frequency ratios.** The map on the left has  $\theta = \omega_{\text{spin}}/\omega_{\text{prec}} = 9.3$ , whose continued fraction representation is  $[9, 3, 3]$ , whereas the lower map has the more irrational ratio  $\theta = 9.61803$ , whose continued fraction representation is  $[9, 1, 1, 1, \dots]$ . A series of Moiré patterns on intermediate angular scales is clearly visible in the map on the left, which lead to spikes in the crossing moment map power spectra, and also in the final bandpass mismatch power spectra. The artefacts can be avoided by choosing ratios of frequencies judiciously in order to avoid good rational approximations.

The theory of choosing ratios to avoid near resonances relates to problems well studied by pure mathematicians in the area of number theory, or more specifically the theory of Diophantine approximations, and we discussed these issues in more detail elsewhere [35]. The tool for characterizing the near resonance properties of real numbers is the continued fraction representation, where we expand

$$\theta = [a_0, a_1, a_2, \dots] = a_0 + \frac{1}{a_1 + \frac{1}{a_2 + \dots}} \quad (3.19)$$

where  $a_0$  is an integer and  $a_1, a_2, \dots$  are positive integers. For a rational number, the continued fraction representation terminates; for an irrational number it is of infinite length. The partial sums, known as ‘convergents,’ generate a sequence of ‘best rational approximations’  $p/q$  to  $\theta$ ,<sup>4</sup> with  $q$  ascending. When a coefficient  $a_n$  is large compared to one, the preceding convergent is a particularly good approximation to  $\theta$  considering the magnitude of  $q$ . The Golden ratio  $\Phi$  has the continued fraction representation  $[1, 1, 1, \dots]$ , and thus has among the worst approximation properties of any number.

For the parameters used in the simulations reported below, we adjusted the precession period so that there are an integer number 5467 cycles in a sidereal year, giving a precession period of 96.2080 minutes, and we replaced the ratio of  $\theta = 9.3$ , which in terms of continued fractions is represented by  $[9, 3, 3]$ , with the ratio 9.618033988749895,<sup>5</sup> whose continued fraction representation is  $[9, 1, 1, 1, \dots]$ , giving a spin period of 10.002876 minutes. One may

<sup>4</sup>An irreducible fraction  $p/q$  is a ‘best approximation’ to  $\theta$  if  $|\theta - p'/q'| > |\theta - p/q|$  whenever  $q' < q$ .

<sup>5</sup>In any specific application, the objective of avoiding near resonances obviously requires an accuracy involving only a finite number of terms of the continued fraction expansion. Moreover, it is less the instantaneous ratio of frequencies that matters but rather the relative phase. We have found using numerical simulations that avoiding Moiré patterns is achieved when the ratios are maintained with a relative accuracy of 1 part in  $10^3$ , although the exact accuracy needed will depend on the particular application.

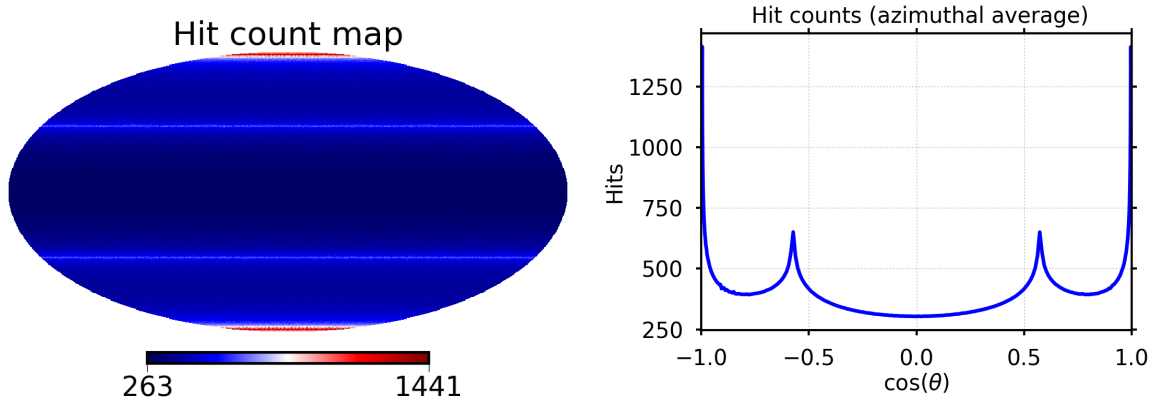


**Figure 13. Hitcount map and azimuthal average for fiducial scanning pattern** The hitcount map is roughly uniform except for some localized spikes of high density around the ecliptic poles and at the caustics at ecliptic latitude  $\pm(\alpha - \beta) = \pm(65^\circ - 30^\circ) = \pm 35^\circ$ . In the bottom plot the horizontal axis is  $\cos \theta$  where  $\theta$  is the angle from the north ecliptic pole.

ask: approximately to what accuracy would one wish to maintain this ratio? Certainly more accuracy than the inverse of the number of precession cycles in a year would be superfluous. In fact, less accuracy would be adequate, the exact number depending on the precise scanning parameters, but we postpone further assessment of the required precision to future work. Moreover, it is more the absolute pointing that matters and not so much a question of maintaining precise ratios at any particular moment.

An important practical question is what accuracy is required in the ratios of the frequencies in order to avoid the Moiré patterns due to near resonances. It is not possible to provide a general answer to this question, but we performed some numerical experiments for the scanning frequencies considered in this paper and found that tuning the ratio of the frequencies to about 0.2% sufficed. It should be stressed that it is the relative phase rather than the instantaneous ratio of frequencies that matters for avoiding Moiré artifacts. In the above discussion we considered only a single ratio, but for more complicated situations with several frequencies, there is more than one ratio to keep away from near resonant values. A rotating half-wave plate, for example, introduces another frequency, and in principle the annual drift also allows other dimensionless ratios of frequencies to be formed. These complications will be investigated elsewhere.

### 3.4 Hitcount and crossing moment map properties

We now examine the properties of the hitcount map  $H_a(p)$  for a particular detector labeled by the index  $a$  (where the index  $p$  denotes a particular discrete pixel) as well as maps of  $\langle \cos 2\psi(p) \rangle_a$ ,  $\langle \sin 2\psi(p) \rangle_a$ ,  $\langle \cos 4\psi(p) \rangle_a$ , and  $\langle \sin 4\psi(p) \rangle_a$ , which, as already stressed enter into the expressions for the bandpass mismatch.

Figures 13 and 14 show the maps  $H_a(p)$ ,  $\langle \cos 2\psi(p) \rangle_a$ ,  $\langle \sin 2\psi(p) \rangle_a$ ,  $\langle \cos 4\psi(p) \rangle_a$ , and  $\langle \sin 4\psi(p) \rangle_a$  for a typical detector with the fiducial scan parameters given above for a full-year scan (so that there are no boundaries).

These figures demonstrate that in all the maps (except for the  $\langle \sin 2\psi(p) \rangle_a$ , and  $\langle \sin 4\psi(p) \rangle_a$  maps), when small-scale structure is ignored, there is an azimuthally symmetric non-uniformity. From the azimuthally averaged quantities shown in Fig. 2, we can see that superimposed on

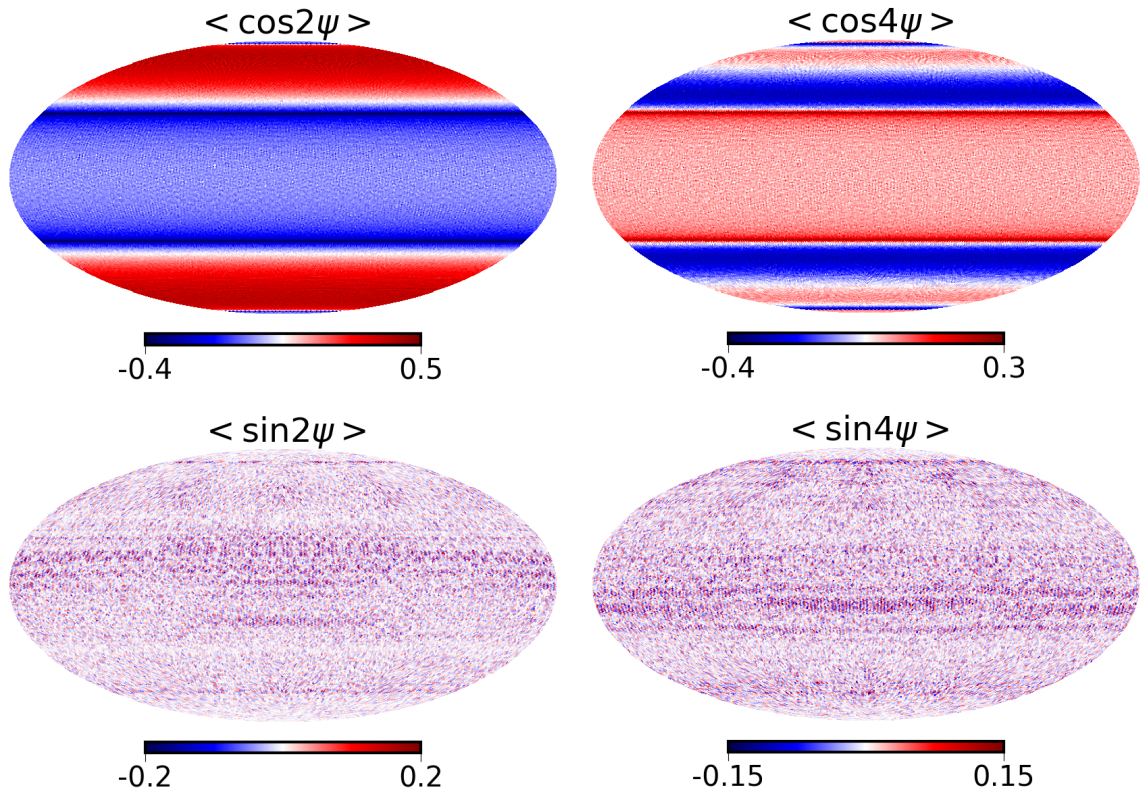


**Figure 14. Crossing moment maps for the fiducial scanning pattern.** The four relevant crossing moment maps  $\langle \cos 2\psi \rangle$ ,  $\langle \cos 4\psi \rangle$ ,  $\langle \sin 2\psi \rangle$ ,  $\langle \sin 4\psi \rangle$  (left to right, top to bottom) are shown for the fiducial scanning pattern (defined in the text) for a single detector whose polarization axis is oriented along the line running from the center of the beam to the spin axis. The corresponding maps for other polarizer orientations can be obtained trivially using the property that the first two maps transform as a spin-2 vector and the second two as a spin-4 vector under rotations of the polarization orientation. We observe that the cosine maps have structures coherent on large scales and azimuthally symmetric in ecliptic coordinates, whereas the sine maps include only small-scale noise (which is also present in the cosine maps) but have no structure coherent on large angular scales.

this azimuthally symmetric component is a component almost completely devoid of large-angle power resulting from the discreteness of the scans. Fig. 15 shows the power spectra of the crossing moment maps. We note that given the finite size of the focal plane, the spin opening angle  $\beta$  varies from detector to detector. This variation in  $\beta$  induces an azimuthally symmetric component having large-scale power in the difference map of moments for different detectors at different locations in the focal plane. Also present will be a small-scale component, which would disappear in the limit  $\omega_{\text{spin}}, \omega_{\text{prec}} \rightarrow +\infty$  along with the sampling rate while keeping the ratio  $\omega_{\text{spin}}/\omega_{\text{prec}}$  fixed. This small scale power is somewhat akin to shot noise.

We now consider the effect of a continuously rotating HWP on the second- and fourth-order crossing moment maps, as shown in Figs. 16 and 17. We see that the azimuthally symmetric structures coherent on large angular scales disappear as a consequence of the continuously rotating HWP. The main consequence is to beat down by many orders of mag-



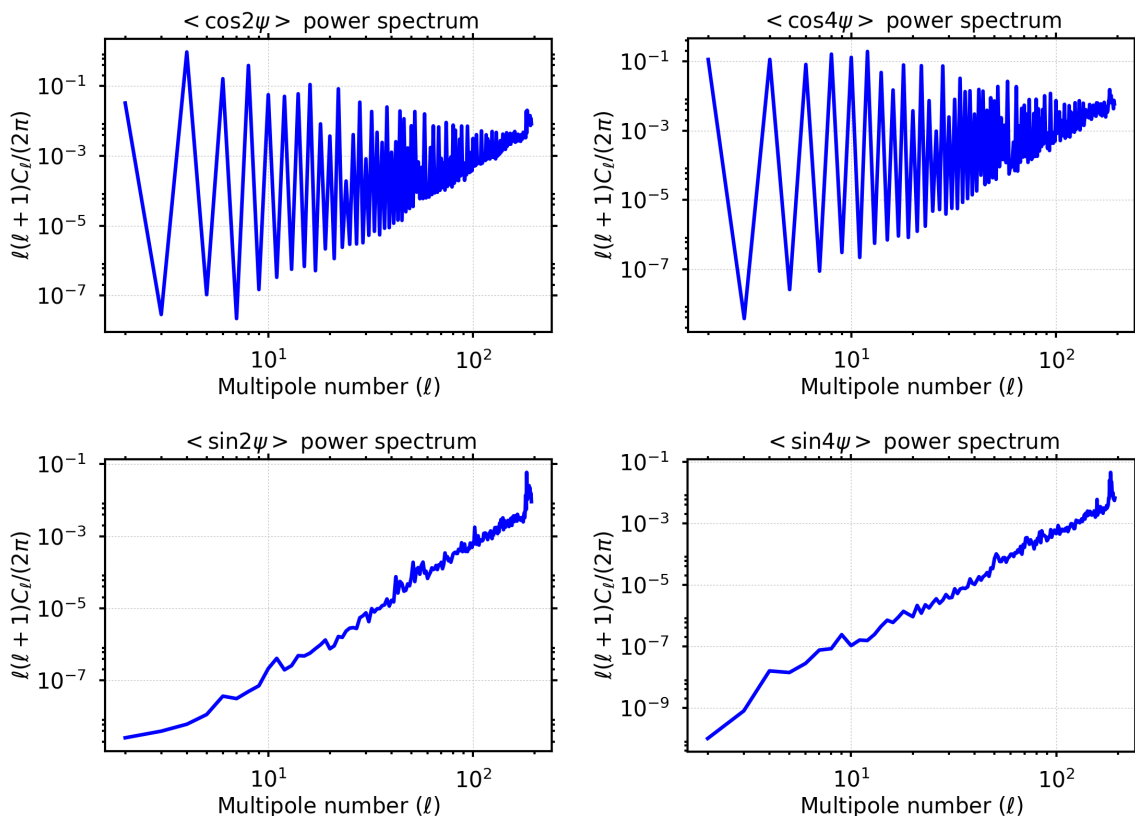


**Figure 15. Crossing moment map power spectra.** We show the power spectra of the maps of Fig. 14. The spectra of the two cosine maps, because of the azimuthally symmetric large power coherent on large scales shown in Fig. 2, have power spectra scaling similar to  $\ell^{-2}$  for the even moments, whereas the two sine maps (bottom) row exhibit spectra resembling pure white noise.

nitude the  $(\ell^{-2.5})$ -like power present on large angular scales in cosine maps, but there is also substantial reduction in the power at all multipole numbers compared to the no-HWP case.

We point out that much the same beneficial effect could also be obtained using a discretely stepped HWP (with a stepping pattern tailored to produce the necessary cancellations). Alternatively, less complete cancellations could also be obtained by stepping the orientation of the focal plane about its optical axis. These rotations are called “deck rotations” in the BICEP2 papers (see e.g., [8]), a terminology that we shall also adopt. Allowing for such deck rotations, however, would also require additional complexity in the satellite design beyond the simplest no HWP design. Moreover, for the deck rotations alone, the cancellations would be imperfect because the values of  $\beta$  for the individual detector scanning patterns change as the focal plane is rotated (except possibly for one detector situated at the optical axis, assumed to coincide with the deck rotation axis).

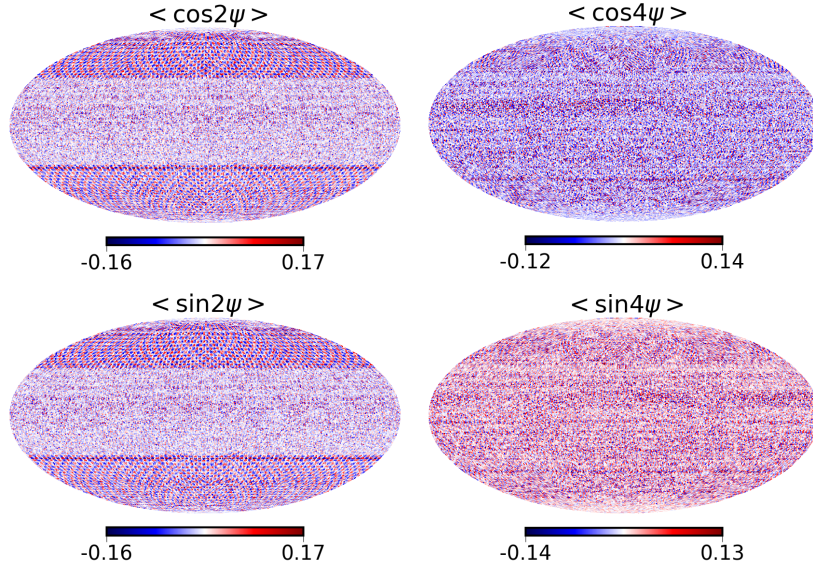


**Figure 16. Crossing moment maps (with rotating HWP).** We show the same maps as in Fig. 14 except that there is a rotating HWP, as explained in the main text. We observe that the coherent power in the cosine maps has been scrambled as a result of the presence of the HWP and the overall power in all the maps has greatly been reduced.

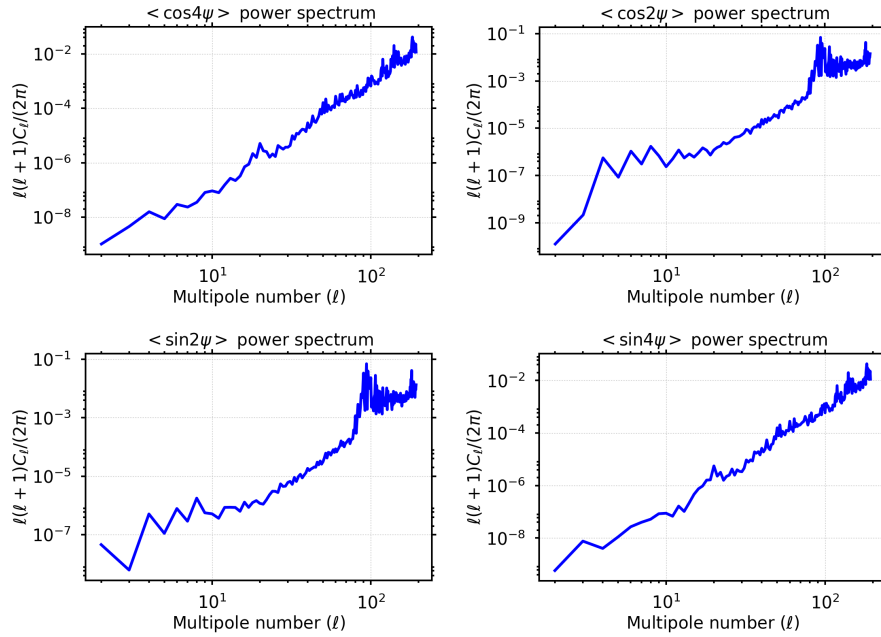


**Figure 17. Crossing moment map power spectra (with rotating HWP)** We show the power spectra for the maps in Fig. 16. The power spectra of the  $\langle \cos 2\psi \rangle$  and  $\langle \cos 4\psi \rangle$  have a white noise-like spectrum rather than an  $(\ell^{-2})$ -like spectrum because the HWP has scrambled on large-scale coherent azimuthally symmetry present in the case with no HWP.

## 4 Conclusions

This paper presented estimates of the contribution of bandpass mismatch error to the final determination of the tensor-to-scalar ratio  $r$ , both for the window situated at the ‘re-ionization bump,’ and for the window at the ‘recombination bump’, for a set of observation strategies considered for future CMB polarization experiments. In the case without a HWP, requiring in the optimal case the combination of multi-detector data, we show that the bandpass mismatch error in polarization has a red power spectrum resembling  $\ell^{-2.5}$ . The contribution to  $r$  is of the order of  $10^{-3}$  at the reionization bump, assuming random variations of the detector filters for typical arrays at 140 GHz, such that the variation of the dust component amplitude is of the order of 0.6%. However, with a continuously rotating HWP the spectrum is similar to that of white noise, with the power on the largest scales many orders of magnitude smaller than without a HWP. This is due to the fact that an ideal HWP allows nearly uniform angle coverage in each pixel, and hence the multi-detector solution is almost equivalent to the combination of single detector maps of  $Q$  and  $U$ . The HWP also cancels correlations in the non-uniformity in the angular coverage between different pixels, hence the efficient reduction in power of the bandpass mismatch on large angular scales. We further note that a stepped HWP would reduce bandpass mismatch in a similar way provided that its discrete rotations are properly synchronized with the scan pattern. We show that even with a simplistic multi-detector map-making approach, the HWP suppresses the bandpass leakage power by several orders of magnitude on large scales. We note however that this conclusion ignores the problem of HWP imperfections, in particular chromaticity effects, which would generate bandpass mismatch systematics of its own.

To obtain accurate estimates of the bandpass mismatch error, more precise information would be needed concerning (1) the scan pattern assumed, (2) the variations in the bandpass functions from detector to detector, and/or as the HWP rotates in case such a modulation is implemented, and (3) the foreground removal process. For (1) we used one of the LiteBIRD candidate scan patterns. Likewise, for (2) we based our model for variations in the bandpass function from preliminary results that have actually been achieved in the laboratory between different detectors without a HWP, but there may be effects not properly taken into account that could lead to larger errors, or conversely further technological development could lead to reduced mismatch between bandpass functions. With respect to (3), we simply calculated the bandpass error in a 140 GHz map, assuming that but for this error, the dominant dust and synchrotron components could be removed by subtraction using a perfect foreground component templates. This is certainly a simplification which provides a simple estimate that can be described in a simple term. If the foregrounds turn out to be very complicated, the CMB clean map might be the result of a linear combination of maps whose coefficients (or varying sign) are much larger than one (assuming the maps are normalized to the CMB). A foreground cleaning of this sort (if necessary) may lead to larger bandpass errors than our estimate. Finally, we mention one caveat of our analysis: we did not include  $1/f$  noise in our modeling, a feature that allowed us to carry out pixel-by-pixel map making and avoid including extra model parameters.

In this paper we have estimated bandpass mismatch error assuming that no measures have been taken to correct for or otherwise mitigate this systematic error. In the companion paper Ref. [19] we explore paths to correct for and mitigate bandpass mismatch error with a dedicated data processing step.

## Acknowledgments

Duc Thuong Hoang thanks the Vietnam International Education Cooperation Department (VIED) of the Ministry of Education and Training for support through a Ph.D. fellowship grant. We thank Aritoki Suzuki for useful discussions and sharing with us data on filter bandpass measurements.

## References

- [1] Planck Collaboration I, *Planck early results. I. The Planck mission*, *A&A* **536** (2011) A1.
- [2] C. L. Bennett et al., *Nine-year Wilkinson Microwave Anisotropy Probe (WMAP) Observations: Final Maps and Results*, *ApJS* **208** (2013) 20, [[1212.5225](#)].
- [3] Planck Collaboration, *Planck 2015 results. XI. CMB power spectra, likelihoods, and robustness of parameters*, *A&A* **594** (2016) A11, [[1507.02704](#)].
- [4] T. Louis et al., *The Atacama Cosmology Telescope: two-season ACTPol spectra and parameters*, *JCAP* **6** (2017) 031, [[1610.02360](#)].
- [5] A. T. Crites et al., *Measurements of E-Mode Polarization and Temperature-E-Mode Correlation in the Cosmic Microwave Background from 100 Square Degrees of SPTpol Data*, *Astrophys. J.* **805** (2015) 36, [[1411.1042](#)].
- [6] Polarbear Collaboration, *A Measurement of the Cosmic Microwave Background B-mode Polarization Power Spectrum at Sub-degree Scales with POLARBEAR*, *Astrophys. J.* **794** (2014) 171, [[1403.2369](#)].
- [7] R. Keisler et al., *Measurements of Sub-degree B-mode Polarization in the Cosmic Microwave Background from 100 Square Degrees of SPTpol Data*, *Astrophys. J.* **807** (2015) 151, [[1503.02315](#)].
- [8] BICEP2 and Keck Array Collaborations, *BICEP2/Keck Array V: Measurements of B-mode Polarization at Degree Angular Scales and 150 GHz by the Keck Array*, *Astrophys. J.* **811** (2015) 126, [[1502.00643](#)].
- [9] BICEP2/Keck and Planck Collaborations, *Joint Analysis of BICEP2/Keck Array and Planck Data*, *Phys. Rev. Lett.* **114** (2015) 101301, [[1502.00612](#)].
- [10] BICEP2 Collaboration and Keck Array Collaboration, *Improved Constraints on Cosmology and Foregrounds from BICEP2 and Keck Array Cosmic Microwave Background Data with Inclusion of 95 GHz Band*, *Phys. Rev. Lett.* **116** (2016) 031302, [[1510.09217](#)].
- [11] J. Delabrouille et al., *Exploring Cosmic Origins with CORE: Survey requirements and mission design*, *ArXiv e-prints* (2017) , [[1706.04516](#)].
- [12] M. Hazumi et al., *LiteBIRD: a small satellite for the study of B-mode polarization and inflation from cosmic background radiation detection*, *Proc. SPIE* **8442** (2012) 844219.
- [13] T. Matsumura et al., *LiteBIRD: Mission Overview and Focal Plane Layout*, *J. Low. Temp. Phys.* **184** (2016) 824–831.
- [14] A. Kogut, J. Chluba, D. J. Fixsen, S. Meyer and D. Spergel, *The primordial inflation explorer (PIXIE)*, *Proc. SPIE* **9904** (2016) 99040W–99040W–23.
- [15] Planck Collaboration, *Planck intermediate results. XLVI. Reduction of large-scale systematic effects in HFI polarization maps and estimation of the reionization optical depth*, *A&A* **596** (2016) A107, [[1605.02985](#)].
- [16] E. Komatsu et al., *Results from the Wilkinson Microwave Anisotropy Probe*, *Prog. Th. Exp. Phys.* **2014** (2014) 06B102, [[1404.5415](#)].

- [17] T. Essinger-Hileman et al., *Systematic effects from an ambient-temperature, continuously rotating half-wave plate*, *Review of Scientific Instruments* **87** (2016) 094503, [[1601.05901](#)].
- [18] T. Matsumura, *A cosmic microwave background radiation polarimeter using superconducting magnetic bearings*. PhD dissertation, University of Minnesota, Minnesota, USA, 2006.
- [19] R. Banerji et al., *Bandpass mismatch error for satellite CMB experiments II: Correcting the spurious signal, in preparation* .
- [20] Planck Collaboration, *Planck 2013 results. XIII. Galactic CO emission*, *A&A* **571** (2014) A13, [[1303.5073](#)].
- [21] Planck Collaboration, *Planck 2013 results. XI. All-sky model of thermal dust emission*, *A&A* **571** (2014) A11, [[1312.1300](#)].
- [22] Planck Collaboration, *Planck intermediate results. XXII. Frequency dependence of thermal emission from Galactic dust in intensity and polarization*, *A&A* **576** (2015) A107, [[1405.0874](#)].
- [23] Planck Collaboration, *Planck 2015 results. X. Diffuse component separation: Foreground maps*, *A&A* **594** (2016) A10, [[1502.01588](#)].
- [24] Planck Collaboration, *Planck 2013 results. IX. HFI spectral response*, *A&A* **571** (2014) A9, [[1303.5070](#)].
- [25] Planck Collaboration, *Planck 2015 results. VIII. High Frequency Instrument data processing: Calibration and maps*, *A&A* **594** (2016) A8, [[1502.01587](#)].
- [26] N. Jarosik et al., *Three-Year Wilkinson Microwave Anisotropy Probe (WMAP) Observations: Beam Profiles, Data Processing, Radiometer Characterization, and Systematic Error Limits*, *ApJS* **170** (2007) 263–287, [[astro-ph/0603452](#)].
- [27] B. Westbrook et al., *Development of the Next Generation of Multi-chroic Antenna-Coupled Transition Edge Sensor Detectors for CMB Polarimetry*, *J. Low. Temp. Phys.* **184** (2016) 74–81.
- [28] Planck Collaboration et al., *Planck intermediate results. XLVI. Reduction of large-scale systematic effects in HFI polarization maps and estimation of the reionization optical depth*, *A&A* **596** (2016) A107, [[1605.02985](#)].
- [29] J. Bock et al., *Study of the Experimental Probe of Inflationary Cosmology (EPIC)-Intermediate Mission for NASA’s Einstein Inflation Probe*, *ArXiv e-prints* (2009) , [[0906.1188](#)].
- [30] K. M. Górski et al., *HEALPix: A Framework for High-Resolution Discretization and Fast Analysis of Data Distributed on the Sphere*, *Astrophys. J.* **622** (2005) 759–771, [[astro-ph/0409513](#)].
- [31] F. Couchot, J. Delabrouille, J. Kaplan and B. Revenu, *Optimised polarimeter configurations for measuring the Stokes parameters of the cosmic microwave background radiation*, *A&AS* **135** (1999) 579–584, [[astro-ph/9807080](#)].
- [32] H. Ishino et al., *LiteBIRD: lite satellite for the study of B-mode polarization and inflation from cosmic microwave background radiation detection*, *Proc. SPIE* **9904** (2016) 99040X.
- [33] M. Bucher et al., *in preparation* .
- [34] C. G. R. Wallis, M. L. Brown, R. A. Battye and J. Delabrouille, *Optimal scan strategies for future CMB satellite experiments*, *MNRAS* **466** (2017) 425–442, [[1604.02290](#)].
- [35] M. Bucher, *Maximum irrationality for optimal scanning of the CMB Sky, in preparation* .